Check for updates

Water Resources Research

RESEARCH ARTICLE
10.1029/2021WR030248

Special Section:
Advancing process representation in hydrologic models: Integrating new concepts, knowledge, and data

Cross-Validating Hydromechanical Models and Tracer Test Assessments of Hyporheic Exchange Flow in Streams With Different Hydromorphological Characteristics

I. Morén[1], J. Riml[1], and A. Wörman[1]

[1]KTH Royal Institute of Technology, Stockholm, Sweden

Key Points:

- An inductive and a deductive approach for estimating hyporheic exchange velocity were cross-validated in streams of varying hydromorphology
- Longitudinal variation in the water surface profile constituted a major control of hyporheic exchange flow (HEF) in the investigated streams
- Spatial scales smaller than five meters are likely important to consider to satisfactory quantify HEF in small streams

Supporting Information:

Supporting Information may be found in the online version of this article.

Correspondence to:

I. Morén,
imoren@kth.se

Citation:

Morén, I., Riml, J., & Wörman, A. (2021). Cross-validating hydromechanical models and tracer test assessments of hyporheic exchange flow in streams with different hydromorphological characteristics. *Water Resources Research*, *57*, e2021WR030248. https://doi.org/10.1029/2021WR030248

Received 20 APR 2021
Accepted 11 NOV 2021

Author Contributions:

Conceptualization: I. Morén, J. Riml, A. Wörman
Data curation: I. Morén, J. Riml
Formal analysis: I. Morén
Funding acquisition: A. Wörman
Investigation: I. Morén

© 2021 The Authors.
This is an open access article under the terms of the Creative Commons Attribution-NonCommercial License, which permits use, distribution and reproduction in any medium, provided the original work is properly cited and is not used for commercial purposes.

Abstract Hyporheic exchange flow (HEF) can generally be quantified through two different approaches. The first approach, which is deductive, entails physically based models, supported with relevant observations. The second approach includes inductive assessments of stream tracer tests using solute transport models, which provide a useful mathematical framework that allows for upscaling of results, but included parameters often have a vague physical base, which limits the possibilities of generalizing results using independent hydromorphological observations. To better understand how the physical basis of HEF-quantifying parameters relates to stream hydromorphology at different spatial scales, we cross-validated the results from (a) tracer test assessments using a 1D solute transport model that accounts for HEF and (b) an independent hydromechanical model that represents HEF driven by multiscale pressure gradients along the streambed interface. To parameterize the models, topographical surveys, tracer tests, and streambed hydraulic conductivity measurements were performed in 10 stream reaches, differing in terms of geomorphology, slope, and discharge. The results show that the models were cross-validated in terms of the average exchange velocity, providing a plausible physical explanation for this parameter in small alluvial streams with low discharges, shallow depth, and moderate slopes. However, the hydromechanical model generally resulted in wider residence time distributions and occasionally higher average residence times compared to the tracer test assessments. From the cross-validated multiscale hydromechanical model, we learned that water surface profile variations were the main drivers of HEF in all investigated streams and that spatial scales between 20 cm and 5 m dominated the estimated HEF velocity.

1. Introduction

Hyporheic exchange flow (HEF) is the flow of surface water in streams and rivers that enters the subsurface zone, and after some time, returns to the surface (e.g., Boano et al., 2014; Cardenas, 2015; Harvey & Bencala, 1993). Since hyporheic exchange velocities are considerably slower than the surface water velocity, HEF causes retention of stream water and solutes traveling with the water (e.g., Cardenas, 2008; Runkel, 2002; Wörman et al., 2002). Furthermore, this mixing zone of groundwater and surface water provides essential habitats for many types of benthic organisms and enhances biogeochemical reactions (e.g., Boano et al., 2014; Jones & Mulholland, 2000). Even though great progress has been made to understand the hyporheic zone and its impact on transport in streams and rivers, previous research on HEF has struggled to progress from interpreting relevant processes to predicting them under different conditions (Ward & Packman, 2019), which could be valuable for well-targeted stream restoration efforts (Dufour & Piégay, 2009; Ward et al., 2001). One obstacle to overcome to achieve such an advancement, as identified in Ward and Packman (2019), relates to the poorly understood scale dependency of HEF, where the subsurface flow observed at a specific point in the landscape is part of a hierarchic flow system that acts within a wide range of spatial and temporal scales (Tóth, 1963; Wörman et al., 2007). Another obstacle relates to the site- and time-specific nature of in situ observations of hyporheic exchange, which makes it complicated to compare results from different studies and to move forward toward a more common conceptual understanding of HEF.

Among other methods, in-stream tracer tests have traditionally been used to quantify HEF. The tracer tests are evaluated using solute transport models, which conceptualize HEF as a temporary storage of stream water flow. Tracer tests are a direct measurement of the fate of conservative or reactive solutes at the reach scale, which is valuable information, for example, for water managers. Furthermore, the mathematical framework of a solute transport model provides means for upscaling and implementation of the results in compartment stream network

Methodology: I. Morén, J. Riml, A. Wörman
Supervision: I. Morén, J. Riml, A. Wörman
Visualization: I. Morén
Writing – original draft: I. Morén
Writing – review & editing: J. Riml, A. Wörman

models (Riml & Wörman, 2011). Early developed transport models with temporal storage assumed that the main channel was connected to a well-mixed transient storage zone and that there was a first-order transport of mass between the two zones (Bencala & Walters, 1983). Furthermore, the considerably lower transport times in the storage zone compared to those in the main channel were defined by an exponential residence time distribution (RTD). Subsequently, model development led to a relaxation of the exponential RTD. Instead, numerous models has been proposed in which the associated predefined RTD, in one or several storage zones, has been allowed to take other statistical forms (e.g., Briggs et al., 2009; Gooseff et al., 2003; Haggerty et al., 2002; Wörman et al., 2002). However, as the number of model parameters increases, the model calibration toward tracer test breakthrough curves (BTCs) may improve, but the prediction uncertainty worsens due to non-uniqueness of parameter values and equifinality. To obtain reliable model parameter sets, there is thus a need to perform independent measurements of some of the included parameters to constrain the model (Bottacin-Busolin, 2019; Briggs et al., 2009). Furthermore, regardless of the complexity, solute transport models often suffer from a somewhat unclear physical basis for the HEF-characterizing parameters, which prevents parameters estimated in one stream from being readily transferred to other streams or even the same stream in another hydraulic regime (Harvey et al., 2003, 1996; Knapp & Kelleher, 2020).

Previous studies have related HEF parameters in solute transport models to physical stream characteristics that can be measured in situ, using scaling laws. The average hyporheic residence time has for example, been related to the Froude number (Salehin et al., 2003; Sawyer et al., 2011; Wörman et al., 2002) and to measures of geomorphological complexity such as reach slope, streambed concavity, and sinuosity (Boano et al., 2006; Gooseff et al., 2007). Measures that reflect both geomorphology and in-stream hydraulics, such as stream power and the Darcy-Weisbach friction factor, have also been shown to be useful for explaining HEF parameters (Harvey et al., 2003; Zarnetske et al., 2007). Furthermore, in conditions where turbulent diffusion composes an important exchange mechanism, the exchange rate has been related to different versions of the Reynolds number (Grant et al., 2018; O'Connor & Harvey, 2008; Packman et al., 2004). Another suggestion for an improved conceptual understanding and a better physical explanation for HEF parameters in solute transport models is to compare model parameters assessed from tracer tests with other models, preferably models with a clear physical basis (Knapp & Kelleher, 2020).

In contrast to the inductive approach of assessing tracer tests using general solute transport models to quantify HEF, a deductive approach is to use physically based models that centers on physical laws and assumptions regarding the main mechanisms controlling hyporheic exchange (Boano et al., 2014). Under steady conditions, the most investigated control of HEF is the longitudinal variation in the hydraulic head at the streambed interface, which is often divided into a static part and a dynamic part. The static head part represents the effect of streambed elevation and stream depth, and the dynamic head part represents the conversion of the velocity head to the pressure head due to the water flow acceleration at the streambed (Boano et al., 2014). Although the research community has a conceptual idea regarding in which type of conditions static or dynamic head gradients predominate, there is no clear method for describing the transformation from dominance of one head type to dominance of another head type in natural streams (Tonina & Buffington, 2007; Wondzell et al., 2019). Since these two mechanisms occur simultaneously and scale differently with discharge and geomorphology, it is important to consider both to obtain functional scaling laws or parameterization methods for HEF parameters in general solute transport models. Furthermore, to capture the entire distribution of hyporheic pathways observed with a tracer test, the multiscale nature of hyporheic exchange can probably not be disregarded.

The fact that HEF occurs over a wide range of spatial scales can be considered through spectral analysis of geomorphological data, which makes it possible to identify periodicity within a data series and to understand the importance of different spatial scales by the decomposition of the data series into simpler parts. Using this approach, an exact solution to groundwater flow, including HEF, was presented in Wörman et al. (2006). The model was based on superpositioning principles, and the hydraulic head boundary condition at the streambed interface was expressed by a real Fourier sum. This modeling approach, or slightly modified versions, has subsequently been applied to study HEF in many different settings, such as in natural streams (Marzadri et al., 2014; Mojarrad et al., 2019; Morén et al., 2017; Stonedahl et al., 2012), in flumes (Aubeneau et al., 2015; Lee et al., 2020), and along generic reaches (Herzog et al., 2019). A few previous studies have compared the spectral method with tracer test evaluations and have achieved good results. In Wörman et al. (2006), the hyporheic zone RTD was derived with a particle tracking routine through the calculated velocity field of a 50 m long reach of Sugar Creek,

19447973, 2021, 12, Downloaded from https://agupubs.onlinelibrary.wiley.com/doi/10.1029/2021WR030248 by Statens Beredning, Wiley Online Library on [28/01/2024]. See the Terms and Conditions (https://onlinelibrary.wiley.com/terms-and-conditions) on Wiley Online Library for rules of use; OA articles are governed by the applicable Creative Commons License

19447973, 2021, 12, Downloaded from https://agupubs.onlinelibrary.wiley.com/doi/10.1029/2021WR030248 by Statens Beredning, Wiley Online Library on [28/01/2024]. See the Terms and Conditions (https://onlinelibrary.wiley.com/terms-and-conditions) on Wiley Online Library for rules of use; OA articles are governed by the applicable Creative Commons License

Indiana, U.S.A, showing agreement with the RTD obtained from a tracer test evaluation. Furthermore, the hyporheic exchange velocity calculated using a physical, multiscale model was slightly lower than the equivalent parameter evaluated from a tracer test in a small, Swedish, agricultural stream (Morén et al., 2017). Additionally, in Stonedahl et al. (2012), a developed mechanistic model was tested in a real stream and compared with a tracer test, showing that the mechanical model results agreed well with the tracer test results, although the former approach captured longer timescales. A general limitation of physically based models is the large amount of data that are often needed to parameterize them, and the subsequent difficulty of capturing head gradients over short spatial scales. With a multiscale model approach, scales smaller than the measured scales can possibly be included by assuming that the fractal streambed geomorphology can be extrapolated over the non-measured scales (Mojarrad et al., 2019; Morén et al., 2017).

The aim of this study was to cross-validate two common but fundamentally different methods to evaluate key HEF parameters in 10 small Swedish streams with different hydrogeomorphological characteristics. The first method consisted of stream tracer test assessments using a general solute transport model accounting for HEF, specifically, the advective-storage-path (ASP) model developed in Wörman et al. (2002). The second method is based on measurements of topography and surface water elevation, which served as input for a 2D semi-analytical hydromechanical (HM) model, describing HEF across a multitude of spatial scales (Morén et al., 2017; Wörman et al., 2006). The term cross-validation here refers to testing the possibility of agreement between those two extensively different approaches for calculating HEF, which hypothetically indicates robustness of both approaches and provides a link between the general HEF parameters of the ASP model and the physically based parameters of the HM model in the investigated streams. Because the investigation was performed in 10 different stream reaches with different characteristics, from low-slope agricultural ditches to moderately steep, gravel-bed, forest streams, the comparison adds to the generalization of previous studies and provides an assessment of the model suitability in different types of streams. The second aim of this study was to show how the HM model could account for a decomposition of the HEF across a wide range of spatial scales and the implications this approach had on the cross-validation results. We investigated which spatial scales and HEF drivers are the most important to consider when modeling hyporheic exchange under different conditions and tested the effect of including smaller spatial scales than those measured in the stream.

2. Methods

In this study, hyporheic parameters were derived using two different models that reflect two considerably different approaches to quantify HEF. We used the HM model to deduce HEF parameters from independent data, and the ASP model to induce the same parameters from stream tracer tests. An extensive field survey was performed to collect relevant data for the two approaches. The results were then cross-validated by comparing the deduced HEF parameters with the induced HEF parameters within model sensitivity intervals. The HM model was also utilized to investigate how static and dynamic head driven HEF varies across different spatial scales and between 10 reaches of different hydromorphology.

2.1. Field Measurements and Data Analysis

Field measurements were performed in 10 small Swedish streams with varying characteristics and included rhodamine WT (RWT) tracer tests, topographic surveys and streambed hydraulic conductivity measurements. The reaches, whose length range between approximately 200–500 m, along the stream thalweg, where located in five different catchments. The catchments included both agricultural areas and coniferous and mixed forests, and the stream reaches had different geomorphological characteristics, defined through the average slope, S (−), sinuosity s (−), and qualitative assessments of the streambed material (Table 1).

2.1.1. Tracer Tests

In each stream reach, a tracer test was performed, using RWT and in situ submersible fluorimeters (Cyclops C7, Turner Designs, Inc., U.S.A.). The tracer was added to the stream water column as a slug injection, and two fluorimeters, positioned upstream and downstream of the reach, registered the BTC for at least 48 h. The tracer tests were designed to achieve complete mixing within the stream cross-section at the point of the upstream measuring site and with a duration that allowed for capturing the tails of BTCs. The shape of the BTC tail is expected to reflect the hyporheic exchange process (e.g., Drummond et al., 2012; Haggerty et al., 2002; Wörman, 2002),

19447973, 2021, 12, Downloaded from https://agupubs.onlinelibrary.wiley.com/doi/10.1029/2021WR030248 by Statens Beredning, Wiley Online Library on [28/01/2024]. See the Terms and Conditions (https://onlinelibrary.wiley.com/terms-and-conditions) on Wiley Online Library for rules of use; OA articles are governed by the applicable Creative Commons License

Table 1
*Characteristics of Investigated Stream Reaches in Terms of Stream Hydrogeomorphology, Surrounding Environment, Bed Material, Stream Length (X) and Distance Between Two Measurements of the Topographical Survey (**Δx**)*

	Stream characteristics	Surrounding environment	Bed material	$X\,(\mathrm{m})$	Δx (m)
R1	Sinuous, riffle and pool with occasional cascades, pristine, perennial	Coniferous forest	Sand, gravel, and stones	273	0.5
R2a	Meandering, riffle and pool with occasional cascades, pristine, perennial	Coniferous forest	Sand, gravel, and stones	338	0.5
R2b	Straight, riffle and pool, pristine	Mixed forest	Sand	288	1
R3	Straight, partly channelized with stone walls, occasional steps	Agriculture	Sand and gravel, clay in pools	197	0.5
R4	Sinuous, flat bottom, partly channelized with stone walls	Mixed forest and agriculture	Sand and gravel	578	1
R6a	Straight, riffle and pool, pristine	Coniferous forest	Sand and gravel	386	0.5
R6b	Sinuous, partly dense vegetation	Agriculture	Sand and gravel, clay in pools	495	1
R6c	Straight, riffle and pool, ocational steps, pristine	Mixed forest and agriculture	Sand, gravel and stones, clay in pools	226	0.5
R6d	Straight, channelized, partly dense vegetation	Agriculture	Clay and sand	208	0.5
R7	Straight, riffle and pool	Mixed forest and agriculture	Sand and gravel	204	0.5

which was the focus of this study. The injected mass and distance from the upstream fluorimeter varied among the stream reaches and were decided based on the estimated discharge and stream velocity at the time of the tracer test. The resistivity signal (mV) from the fluorimeters was transformed into the RWT concentration through a standard calibration curve prepared for a relevant concentration range using water from the different streams. In reach R1 and R6b, the upstream standard calibration curves were compromised, and the RWT concentrations were scaled in these streams, to gain 100% mass recovery along the reach and to achieve zero background concentration. The percentage mass recovery was calculated as follows: $100 * Q\int C_{\mathrm{BTC\_down}}(t)dt \,/\, Q\int C_{\mathrm{BTC\_up}}(t)dt$, where $C_{\mathrm{BTC\_up1}}(t)$ and $C_{\mathrm{BTC\_down}}(t)$ are the observed RWT BTCs at the upstream measuring point and downstream measuring point, respectively, and the unknown discharge Q is assumed constant along the reach.

2.1.2. Stream Bottom and Water Surface Profiles

The stream bottom profiles were surveyed using a Leica Sprinter 50 automatic leveling instrument (Leica Geosystems AG, Switzerland) every 0.5 or 1 m depending on the stream reach (Δx in Table 1). To gauge the stream water surface profile (WSP) and the average stream depth, the depth was measured at the same positions as the bottom measurements using a measuring rod. The slope (S) was taken as the linear trend in topography measurements over the entire stream reach, where the length of the stream was taken as that of the thalweg. The height measurements had an instrumental accuracy of 2 mm, and we judged the accuracy of the stream-depth measurements to be ±5 mm. Thus, in total, the WSPs were estimated to have an accuracy of ±7 mm. The exact distance between points could be calculated based on the distance between the digital stage and the leveling instrument and the angle between measured points. Each water elevation profile and stream bottom profile were measured for one or two days, and the respective tracer test was performed in the evening on the first day to ensure that the two methods captured the same hydraulic conditions. None of the profiles or connected tracer tests were performed during rainy conditions or shortly after rainfall; thus, the hydraulic conditions were considered stable. Profiles are presented in Figure S1, in the Supporting Information.

2.1.3. Hydraulic Conductivity

Hydraulic conductivity, $K\,(\mathrm{m/s})$, was measured at four to six cross-sections depending on the length of the stream reach. At each cross-section, measurements were made at three positions across the stream and at two depths (3 and 7 cm) through falling head tests, using a piezometer. According to (Hvorslev, 1951), the flow out of the piezometer at a constant hydraulic head pressure is:

$$q(t) = \pi r^2 \frac{dh(t)}{dt} = FK\left(H_0 - H(t)\right) \tag{1}$$

where r (m) is the radius of the piezometer, $H\,(t)$ (m) is the level of water in the container at the time t (s), and H_0 (m) is the water level at time infinity, that is, at pressure equalization. F (m) is a factor related to the shape

and dimensions of the piezometer opening equal to $F = \frac{2\pi L}{\ln\left(L / r\right)}$, where L (m) is the length of the cylindrical opening. By setting the datum, $H\left(0\right) = 0$, the solution to Equation 1 becomes $\ln\left(\frac{H\left(t\right)}{H_0}\right) = \frac{FK}{\pi r^2}t$. The hydraulic conductivity was evaluated here by plotting $\ln\left(\frac{H\left(t\right)}{H_0}\right)$ as a function of t after observations of the lowering of the water table during a certain time. The piezometer used here has $F = 0.23$ and has been utilized to measure hydraulic conductivity in previous studies (Morén et al., 2017; Riml et al., 2013). The final hydraulic conductivity of each reach was taken as the average of all measurements performed in each reach.

2.2. Tracer Test Evaluation of HEF

2.2.1. The ASP Model

The tracer test assessments were performed using a solute transport model accounting for HEF, which is referred to as the ASP model (Wörman et al., 2002). In the model, HEF is defined as purely advective, according to:

$$\frac{\partial Gn}{\partial t} + \frac{\partial z}{\partial \tau}\frac{\partial G}{\partial z} = 0 \tag{2}$$

where G (kg/m^3) is the solute (bulk) concentration in the hyporheic zone, n (−) is the porosity, τ (s) denotes the time since the water entered the zone and z (m) is the curve-linear streamline coordinate. Accordingly, the solute concentration at a streamline end point, thus at the streambed interface, is denoted $G\left(T,\tau\right)\big|_{\tau=T}$, where T (s) is the total residence time of that streamline. By integrating over all possible streamlines, the flow-weighted average concentration of the water exiting the streambed is obtained according to $\langle G\left(T,\tau\right)\big|_{\tau=T}\rangle = \int_0^\infty G\left(t,\tau\right)\big|_{\tau=T} f\left(T\right)dT$, where $f\left(T\right)$ is the flow-weighted residence time probability density function (PDF). From here on, the flow-weighted average of any parameter will be denoted using squared brackets,$\langle\ldots\rangle = \int_0^\infty \ldots f\left(T\right)dT$. The flow through the hyporheic zone is then coupled with the solute transport in the stream according to:

$$\frac{\partial C}{\partial t} + U\frac{\partial C}{\partial x} - E\frac{\partial^2 C}{\partial x^2} = \frac{P}{A}\frac{1}{2}\langle W\rangle\left(-C\left(t\right) + \langle G\left(t,\tau\right)\big|_{\tau=T}\rangle\right) \tag{3}$$

where C (kg/m^3) is the solute concentration in the main channel at the site x (m), U (m/s) is the average stream velocity in the main channel, E (m^2/s) is the longitudinal dispersion coefficient, P (m) is the wetted perimeter of the main channel and A (m^2) is the cross-sectional area of the stream. The discharge $Q = UA$ (m^3/s) is assumed to vary linearly along the reach according to $Q = Q_0\left(1 + x\theta\right)$, where Q_0 (m^3/s) is the discharge at the upstream end of the reach and θ (1/m) is a dilution parameter. Note that in reach R1 and R6b, full mass recovery was assumed, and the dilution parameter was set to zero. The right-hand side of Equation 3 represents the solute flux across the streambed interface, and it scales linearly with the flow-weighted exchange velocity $\langle W\rangle$. The exchange velocity is defined as the Darcy velocity normal to the streambed according to $W\left(x\right) = V_y\left(x, y = 0\right)n\zeta$, where $V_y\left(x, y = 0\right)$ (m/s) is the vertical pour velocity at the streambed and ζ (−) is a constant that compensates for the fact that all streamlines do not enter the streambed perpendicular to the bed (Wörman et al., 2002). From Equations 2 and 3, it is clear that the hyporheic exchange is controlled by two main properties: how much water enters the hyporheic zone, that is, the average exchange velocity $\langle W\rangle$, and how long it stays there, that is, the residence time PDF, $f(T)$. Therefore, these two parameters were the focus of the comparison between the two models presented in this study. We assumed a log normal distribution of residence times in the hyporheic zone because this has been shown to illustrate the hyporheic exchange patterns well, especially the so-called pumping mechanism (Cardenas & Wilson, 2004; Tonina & Buffington, 2011; Wörman et al., 2002). The distribution was quantified through the average residence time $\langle T\rangle$ and coefficient of variation, $\mathrm{CV}\left[T\right]$ (−), which is a measure of variance independent of the distribution mean. An exact solution to Equations 2 and 3 for a slug release was derived in the Laplace domain in Wörman et al. (2002). The solution is developed for a conservative solute and an instantaneous slug injection of mass M (kg) according to $C\left(x = 0, t\right) = \frac{M}{Q_0} * \delta\left(t\right)$, where $\delta\left(t\right)$ is the Dirac pulse, and is based on the assumption that no solute exists in the stream or streambed prior to the injection ($C\left(x, t = 0\right) = G\left(z, t = 0\right) = 0$). The Laplace transformed concentration in the main channel at point x and time t then becomes:

19447973, 2021, 12, Downloaded from https://agupubs.onlinelibrary.wiley.com/doi/10.1029/2021WR030248 by Statens Beredning, Wiley Online Library on [28/01/2024]. See the Terms and Conditions (https://onlinelibrary.wiley.com/terms-and-conditions) on Wiley Online Library for rules of use; OA articles are governed by the applicable Creative Commons License

$$\bar{C}(x,s) = \frac{M}{Q_0(1+x\theta)} \exp\left[\left(\frac{U}{2E} - \sqrt{\left(\frac{U}{2E}\right)^2 + \frac{p}{E} - \frac{1}{2}\frac{P\langle W\rangle}{AE}\langle e^{-pT} - 1\rangle}\right)x\right] \quad (4)$$

where p is the Laplace parameter and the brackets $\langle \ldots \rangle = \int \ldots f(T)dT$, as noted previously.

2.2.2. Calibration and Sensitivity Analysis of ASP Model Parameters

To estimate the parameter values of the ASP model, a calibration against the RWT BTCs was performed. Before the calibration was performed, the measured BTCs were pre-processed by removing the parts of the tails that were considered below the detection limit. Since fluorimeters detect not only RWT, but also noise in the form of for example, light and turbidity, the detection limit was related to the observed variance in the logarithm of the BTC tail concentration. The variance of the BTC was naturally largest over the BTC peak and then decreased with the florescent concentration. However, as the florescent concentration of the tail approached the detection limit, the variance increased, reaching a plateau that corresponds to the noise of the measurements without effects of the variance of the trend (Figure S2). In reach, R6a, R6b, and R6c, BTC tails were cut slightly earlier than in other reaches because of noise that could be related to researchers walking in the stream while performing other measurements. In reach R2a, R3, and R7, all data were utilized in the calibration, since the plateau was never reached.

In the calibration procedure, parameters Q_0, θ, U, E, $\langle W\rangle$, $\langle T\rangle$, and $\mathrm{CV}\left[T\right]$ were adjusted to minimize the error between the observed BTC and the simulated BTC, which is the BTC computed with Equation 4 and subsequently transformed back to the real domain. The injected mass was known, and we approximated the hydraulic radius $\frac{P}{A}$ with $\frac{1}{d}$ since all studied streams were wide in relation to their depths. To emphasize the tail of the BTC in the calibration procedure, we employed a mixed optimization criterion with an object function that weights the error depending on its position on the BTC (Bottacin-Busolin et al., 2011). In this criterion, peak values on the BTC were compared linearly, while values on the tail and the rising limb were compared in logarithmic form. The threshold between the peak and the rest of the BTC was set to 20% of the highest observed concentration. A more detailed description of the object function and threshold is provided in previous articles (Bottacin-Busolin et al., 2011; Morén et al., 2017; Riml et al., 2013).

We also investigated the sensitivity of the model output to changes in the HEF model parameters. This was done through a Monte Carlo (MC) simulation, where parameters $E, \langle W\rangle, \langle T\rangle$, and $\mathrm{CV}\left[T\right]$ were randomly selected from predefined log normal distributions. Because parameters controlling the bulk transport and the dilution of the solute are usually relatively well defined through tracer tests, they were not included in the analysis, that is, U, Q_0, and θ were kept constant according to the optimized values. The modeled BTC, based on the random combination of parameters, was then compared to the observed tracer test BTC, and the calculated errors were plotted against each parameter in so-called dotty plots (Ward et al., 2017). If the error is relatively constant within the investigated parameter space and the dotty plot shows a wide minimum, the model is insensitive to changes in this parameter. A common reason for uncertain parameter estimation is insensitivity to changes in one or several parameters with respect to the chosen error function. We also defined the parameter sets (E_i,$\langle W\rangle_i$, $\langle T\rangle_i$, and $\mathrm{CV}\left[T\right]_i$) with error $e_i < 1.15 * e_{\min}$ as behavioral, where $e_{\min}$ is the smallest calculated error between the observed and calculated BTC. The behavioral parameter sets produce equally reasonable estimates of the observed BTC, which is a way to quantify the relative certainty of the tracer test calibration without being a formal statistical measure.

Since RWT has been shown to be adsorptive in some stream sediments (Runkel,), an additional sensitivity analysis was performed considering the impact of reversible and irreversible instantaneous adsorption of RWT on the optimized ASP model parameters, and the accumulated mass recovery between two measuring points (Supporting Information, text S1, and Figures S3 and S4). Reversible adsorption was accounted for in the ASP model through a constant equilibrium coefficient defined as $K_B = C_{\text{adsorbed}} / C_{\text{diluted}}$ (e.g., Riml et al., 2013), while irreversible adsorption was defined through the first-order rate coefficient $\lambda_B\left(s^{-1}\right)$ (e.g., Keefe et al., 2004; Runkel,).

19447973, 2021, 12, Downloaded from https://agupubs.onlinelibrary.wiley.com/doi/10.1029/2021WR030248 by Statens Beredning, Wiley Online Library on [28/01/2024]. See the Terms and Conditions (https://onlinelibrary.wiley.com/terms-and-conditions) on Wiley Online Library for rules of use; OA articles are governed by the applicable Creative Commons License

19447973, 2021, 12, Downloaded from https://agupubs.onlinelibrary.wiley.com/doi/10.1029/2021WR030248 by Statens Beredning, Wiley Online Library on [28/01/2024]. See the Terms and Conditions (https://onlinelibrary.wiley.com/terms-and-conditions) on Wiley Online Library for rules of use; OA articles are governed by the applicable Creative Commons License

2.3. The Multiscale HM Approach

The HM model for HEF is an exact solution to the continuity and momentum equations for steady, incompressible groundwater flow in two dimensions. The model acknowledges the geomorphologic complexity of natural streambeds by treating the upper hydraulic head boundary and the resulting multiscale HEF as real-space signals, which are transformed into their power spectral densities and analyzed using power spectral theory. The model was supported by stream measurements independent of the stream tracer tests and thus offered the possibility to cross-validate the two approaches included in this study. To compare the outcome of the HM model with that of the ASP model, we used the HM model to derived both the flow-weighted average exchange velocity $\langle W \rangle$ and the residence time PDF $f(T)$, which are defined by the flow-weighted average residence time $\langle T \rangle$ and the coefficient of variation $\mathrm{CV}[T]$.

2.3.1. Longitudinal Head Variations at the Streambed Interface

The HM model accounts for dynamic and static hydraulic head fluctuations, which are transmitted from the open stream flow as driving boundary conditions of the hyporheic (groundwater) flow. The pressure distribution along the streambed generally consists of a hydrostatic part that represents the WSP and a deviation from the hydrostatic head caused by the curvature of streamlines and stagnation of the open flow exactly at the streambed interface, which can be both positive and negative (Chow, 1959). In this study, the deviation from hydrostatic pressure in a stream cross-section was estimated using an empirically based equation consistent with previous attempts to model multiscale HEF (e.g., Stonedahl et al., 2010). The variation in the total hydraulic head along the streambed, $h(x)$, was defined according to:

$$h(x) = h_s + h_d = y_b(x) + d(x) + C_d(x)\,y_b(x) \tag{5}$$

where the static hydraulic head $h_s = y_b(x) + d(x)$ and $y_b(x)$ is the streambed elevation from a fixed datum. The dynamic head was defined as a scaling of the streambed elevation, $h_d = C_d(x)\,y_b(x)$, where the dynamic head scaling factor, $C_d(x)$, was a modification of Fehlman's constant (Elliott & Brooks, 1997a, 1997b; Fehlman, 1985). The modified version, approximates the bed form height (as part of the hydrodynamic drag) using the standard deviation of the streambed topography and accounts for longitudinal variations in the stream depth, stream cross-sectional velocity, and topography (Stonedahl et al., 2010). This process yields a scaling factor that varies along the reach according to:

$$C_d(x) = \frac{\hat{U}(x)^2}{2g}\frac{0.28}{\sqrt{2}\hat{\sigma}_{y_b}(x)}\begin{cases}\left(\dfrac{2\sqrt{2}\hat{\sigma}_{y_b}(x)\,/\,\hat{d}(x)}{0.34}\right)^{\frac{3}{8}} & 2\sqrt{2}\hat{\sigma}_{y_b}(x)\,/\,\hat{d}(x) \le 0.34 \\ \left(\dfrac{2\sqrt{2}\hat{\sigma}_{y_b}(x)\,/\,\hat{d}(x)}{0.34}\right)^{\frac{3}{2}} & 2\sqrt{2}\hat{\sigma}_{y_b}(x)\,/\,\hat{d}(x) \ge 0.34\end{cases} \tag{6}$$

where $\hat{\sigma}_{y_b}(x)$ (m) is the standard deviation in streambed topography over a small distance, x', here set to 10 m and centralized around x, $\hat{d}(x)$ is the moving average of the stream depth over x' and $\hat{U}(x)$ is the moving average of the stream velocity over x'. Furthermore, the linear variation in stream velocity along the stream thalweg was calculated based on continuity according to $U(x) = \xi Q_0(1 + x\,\theta)\,/\,(w \cdot d(x))$, where both the discharge Q_0 and the proportionality constant θ were evaluated using the ASP model. The factor $\xi = U_{\mathrm{ASP}}\,/\,E[U(x)]$ was introduced to account for an observed underestimation of the actual solute advection velocity, U_{ASP}, due to, for example, stagnant pockets alongside the stream channel that were not accounted for by the variability in the cross-sectional area. $E[\ldots]$ denotes the expected value of the variable within the brackets.

2.3.2. The Flow-Weighted Average Exchange Velocity

The HM model used in this study is based on parallel derivation of the hyporheic exchange velocity in the real and spectral domains. The spectral approach was introduced to study the exchange velocity distributed over different

19447973, 2021, 12, Downloaded from https://agupubs.onlinelibrary.wiley.com/doi/10.1029/2021WR030248 by Statens Beredning, Wiley Online Library on [28/01/2024]. See the Terms and Conditions (https://onlinelibrary.wiley.com/terms-and-conditions) on Wiley Online Library for rules of use; OA articles are governed by the applicable Creative Commons License

wavelengths, which clarifies the types of mechanisms and scales that should be emphasized in measurements and modeling efforts to provide pertinent reach-scale quantifications of HEF.

Before deriving the spectral model, we calculated the multiscale hyporheic exchange velocity in the real domain from an exact solution of the Laplace equation for steady incompressible flow, $\nabla^2 h = 0$ (Wörman et al., 2006). The solution is based on a no-flow boundary at depth $y = -\varepsilon$, specified in hydraulic head as $\frac{dh}{dy}\big|_{y=-\varepsilon} = 0$, and an upper hydraulic head boundary condition stated as a Fourier sum according to:

$$h\left(x, y = 0\right) = \sum_{i=1}^{N} A_{h,i} \sin\left(\frac{2\pi}{\lambda_i} x\right) + S \tag{7}$$

where $A_{h,i}$ and λ_i are the amplitude (m) and wavelength (m), respectively, of harmonic i. S is the slope, as specified previously. The solution to the Laplace equation was combined with Darcy's law to derive the entire hyporheic flow field in two dimensions, that is, along and perpendicular to the average slope of a reach (Supporting Information, text S2). Similar to the ASP model, the hyporheic exchange velocity at the streambed interface was defined as the vertical velocity field component at $y = 0$ according to $W\left(x\right) = \zeta n V_y\left(x, y = 0\right) = \zeta K \frac{dh}{dy}\big|_{y=0}$, where K is the homogenous and isotropic saturated hydraulic conductivity of the streambed and we set the coefficient $\zeta = 1$. The final exchange velocity then becomes a Fourier sum according to:

$$W\left(x\right) = \sum_{i=1}^{N} 2\pi K \frac{A_{h,i}}{\lambda_i} \alpha\left(\lambda_i\right) \sin\left(\frac{2\pi}{\lambda_i} x\right), \tag{8}$$

where the factor is referred to as geological damping (−) and reflects the effects of the impermeable layer at depth $y = -\varepsilon$:

$$\alpha\left(\lambda_i\right) = \frac{1 - \exp\left(-4\pi\varepsilon \,/\, \lambda_i\right)}{1 + \exp\left(-4\pi\varepsilon \,/\, \lambda_i\right)} \tag{9}$$

To average the exchange velocity along the streambed, we recognized that since the wavelengths of the included harmonics are even fractions of the longest wavelength, the flow-weighted average of $W\left(x\right)$ equals its standard deviation along the bed according to $\langle W\left(x\right)\rangle = \sigma_{W(x)}$ (Morén et al., 2017). Furthermore, we utilized that the variance of a signal in space or time can be derived by integrating the power spectral density (PSD) of its constituent frequencies (Stoica & Moses, 1997). Thus, by first deriving the PSD of $W\left(x\right)$ as a function of wavelength, denoted $S_W\left(\lambda\right)$ and in units of $\left(\mathrm{m/s}\right)^2 \,/\, \left(1 \,/\, \mathrm{m}\right)$, the flow-weighted average exchange velocity can be expressed as:

$$\langle W \rangle_{\mathrm{HM}} = \sigma_{W(x)} = \sqrt{\int_{\lambda_{\min}}^{\lambda_{\max}} \frac{S_W\left(\lambda\right)}{\lambda^2} d\lambda} \tag{10}$$

where λ (m) is the wavelength of the spectrum, between $\lambda_{\min} = \Delta x^* \,/\, 2$ and $\lambda_{\max} = X$, where Δx^* is the minimal distance between two observations in the interpolated elevation data (see section 2.3.3), and X is the total length of the reach. The index HM represents the HM model and indicates the difference between this parameterization and the respective parameters of the ASP model (Section 2.2.1). A formal link can be created between the real and spectral representation of the exchange velocity by recognizing that the variance of a real single harmonic function is equal to both the squared amplitude divided by two and the integral of its PSD. This link can be defined both for the hydraulic head and for the exchange velocity according to:

$$\frac{A_h\left(\lambda_i\right)^2}{2} = \Delta\lambda_i \frac{S_h\left(\lambda_i\right)}{\lambda_i^2} \tag{11}$$

$$\frac{A_W\left(\lambda_i\right)^2}{2} = \Delta\lambda_i \frac{S_W\left(\lambda_i\right)}{\lambda_i^2} \tag{12}$$

19447973, 2021, 12, Downloaded from https://agupubs.onlinelibrary.wiley.com/doi/10.1029/2021WR030248 by Statens Beredning, Wiley Online Library on [28/01/2024]. See the Terms and Conditions (https://onlinelibrary.wiley.com/terms-and-conditions) on Wiley Online Library for rules of use; OA articles are governed by the applicable Creative Commons License

where $A_W(\lambda_i) = 2\pi K \frac{A_h(\lambda_i)}{\lambda_i} \alpha(\lambda_i)$ is the amplitude of the velocity spectrum. Equations 11 and 12 were applied to calculate the entire hyporheic flow field from estimations of the hydraulic head power spectrum (Supporting Information, text S3). Furthermore, by rearranging and combining Equations 11 and 12, the hyporheic exchange velocity PSD can be separated into different parts according to:

$$S_W(\lambda) = (2\pi K)^2 \alpha(\lambda)^2 \frac{\left(\gamma_d(\lambda) + \gamma_s(\lambda)\right) S_{y_b}(\lambda)}{\lambda^2} \tag{13}$$

where $S_{y_b}(\lambda)$ is the PSD of the streambed topography (m^3) and $\gamma_d(\lambda)$ (−) and $\gamma_s(\lambda)$ (−) are conversion factors, converting the streambed topography gradients into hydraulic heads. The static conversion factor was defined in line with Mojarrad et al. (2019) according to $\gamma_s(\lambda) = \frac{S_{h_s}(\lambda)}{S_{y_b}(\lambda)}$, where $S_{h_s}(\lambda)$ (m^3) is the PSD of the surface water profile $h_s(x) = y_b(x) + d(x)$. $\gamma_s(\lambda)$ is expected to range from low values at small spatial scales, where bottom topography fluctuations are considerably higher than the overlying WSP, to values approaching 1 at larger spatial scales, where the surface water profile is expected to follow landscape topography variations. We also introduced a dynamic conversion factor according to $\gamma_d(\lambda) = \frac{S_{h_d}(\lambda)}{S_{y_b}(\lambda)}$, where $S_{h_d}(\lambda)$ (m^3) is the PSD of the dynamic head fluctuations $h_s(x) = C_d(x) y_b(x)$. A comparison between γ_d and γ_s will provide information about the relative importance of static and dynamic heads as drivers of HEF across features of different wavelengths, and plotting $S_W(\lambda)$ against wavelength illustrates which spatial scales are most important for the final average exchange velocity, $\langle W \rangle_{HM}$.

2.3.3. Power Spectrum Analysis and the Inclusion of Small Spatial Scales

The three power spectra needed to parameterize Equation 13 (and subsequently Equation 10), that is, the stream bottom elevation PSDs, $S_{y_b}(\lambda)$, the static head PSD, $S_{h_s}(\lambda)$ and the dynamic head PSD, $S_{h_d}(\lambda)$, were estimated based on the surveyed stream geometry and using Welch's method (see the Text S3 in Supporting Information S1). Before the PSDs were estimated, the stream bottom and WSP data were interpolated to provide the necessary equal distance between points, Δx^*. The analysis then resulted in estimated PSDs with a minimum wavelength, $\lambda_{min} = 2\Delta x^*$, between 0.45 and 1.48 m for the different stream reaches. For the main part of the analysis, the original PSDs were used. However, since several studies have shown that spatial scales shorter than a couple of meters might be of great importance for the total hyporheic exchange (Gomez-Velez & Harvey, 2014; Morén et al., 2017; Stonedahl et al., 2013), we also investigated a method to include smaller scales by extrapolation of the PSD to even shorter wavelengths. The method utilized the fact that many natural systems, including streambeds, show fractal behavior over the whole or parts of the measured range (e.g., Aubeneau et al., 2015; Hino, 1968; Turcotte, 1992; Wörman et al., 2007). In other words, the PSD generally follows a power law of the form $S(\lambda) = a\lambda^b$. The power law equation can be used to generalize topographic features outside the observed scale range (Mojarrad et al., 2019; Morén et al., 2017), where a and b are constants. All PSDs evaluated in this study were fractal, with changes in the slope indicating multifractility (Figure S5 in Supporting Information S1). This change in slope was transitional in some cases but observed at approximately $\lambda \approx 7d$, which was suggested as an upper limit for the lowest wavelength range of multifractal streambed PSDs in Hino (1968). We, therefore, used the least squares method to find the linear trend of $S_{y_b}(\lambda < 7d)$, $S_{h_s}(\lambda < 7d)$, and $S_{h_d}(\lambda < 7d)$ when plotted against wavelength in a log-log diagram. In reach R2b, however, no wavelengths lower than $7d$ were measured, and a linear trend for $S_{y_b}(\lambda < 2\,m)$, $S_{h_s}(\lambda < 2\,m)$, and $S_{h_d}(\lambda < 2\,m)$ was instead obtained. Based on the fitted linear trends (Table S1 in Supporting Information S1), the PSDs were extrapolated to a minimum wavelength, λ_{min}, of 1 cm, approximately representing the approximate diameter of gravel or pebbles. Subsequently, we investigated the effect of including the smaller scales on the total $\langle W \rangle_{HM}$ and the ratio $\langle W \rangle_d$ / $\langle W \rangle_s$, where the average static exchange velocity $\langle W \rangle_s$ was calculated by setting $\gamma_d = 0$ in Equation 13, and likewise, the average dynamic exchange velocity $\langle W \rangle_d$ was calculated by setting $\gamma_s = 0$. To further investigate the effect of different scales on the hyporheic exchange velocity, $\langle W \rangle_{HM}$ and $\langle W \rangle_d$ / $\langle W \rangle_s$ were calculated while increasing the upper limit of the integral of Equation 10 from $\lambda_{max} = \lambda_{min}$ to $\lambda_{max} = X$.

19447973, 2021, 12, Downloaded from https://agupubs.onlinelibrary.wiley.com/doi/10.1029/2021WR030248 by Statens Beredning, Wiley Online Library on [28/01/2024]. See the Terms and Conditions (https://onlinelibrary.wiley.com/terms-and-conditions) on Wiley Online Library for rules of use; OA articles are governed by the applicable Creative Commons License

2.3.4. The Residence Time PDF

The distribution of residence times in the HM model was obtained by particle tracking through the 2D velocity field, which is provided in its complete form in the Supporting Information S1. After the velocity field was derived, the particles were released at the top boundary ($y = 0$) every 5 cm along the entire length of each studied reach, and the resolution of the flow field was set to 5 mm. The flow-weighted PDF of residence times was defined according to:

$$f\left(T_j\right) = \frac{f_p\left(T_j\right)W_j\left(T\right)}{\sum_{j=1}^{50}\left[f_p\left(T_j\right)W\left(T_j\right) + f_p\left(T_{j+1}\right)W\left(T_{j+1}\right)\right]\left[T_{j+1} - T_j\right]} \tag{14}$$

where $f_p\left(T_j\right)$ is the geometrically weighted PDF of the hyporheic residence time. The subscript p indicates that $f_p\left(T_j\right)$ was calculated from the ensemble of tracked particles, and the subscript j ranges from 1 to 50 and represents bins in a histogram of the residence times of all tracked particles. Within each bin j, the average residence time and exchange velocity were taken to define the pair T_j and $W\left(T_j\right)$, associated with the probability $f_p\left(T_j\right)$, which was estimated as the number of particles in each bin, normalized with the total number of tracked particles and the width of each bin. We then estimated the mean, μ_T, and the standard deviation, σ_T, representing the continuous flow-weighted PDF, by fitting it to the discrete representation of Equation 14. Finally, the average residence time $\langle T\rangle_{\mathrm{HM}}$ was calculated for a range of residence times between 10 and 106 s.

2.3.5. Sensitivity Analysis of the HM Model

The parametrization of the multiscale model was performed mostly independently from the tracer test evaluation through distributed measurements of the hydraulic conductivity, K, and dense measurements of the streambed elevation $y_b\left(x\right)$ and stream depth $d\left(x\right)$. Elevation and depth measurements were then used together with discharge and velocity estimates from the tracer test to estimate the hydraulic head fluctuations (Section 2.3.1) and the associated PDFs (Section 2.3.4). Because the geologic factors, that is, porosity n and depth of a streambed stratum ε, were not measured in situ, we tested the model sensitivity to relevant ranges of those parameters. Values of n were set to 0.2, 0.3, 0.4, and 0.5, with the smallest representing unsorted gravel and the largest representing clay or packed moraine. The range of ε was set between 0.01 and 1 m, which are depths that have been observed in previous tracer studies when approximating the depth with $\varepsilon = \langle W\rangle\langle T\rangle$ / 2 (Morén et al., 2017). The resulting ranges of $\langle W\rangle_{\mathrm{HM}}$ and $\langle T\rangle_{\mathrm{HM}}$ were compared to optimized and behavioral values of $\langle W\rangle_{\mathrm{ASP}}$ and $\langle T\rangle_{\mathrm{ASP}}$.

2.4. Cross-Validation of the HM Model and the Tracer Test Assessment

To quantify the cross-validation of the HM model and the tracer test assessment, we defined and minimized an error that considered both the average exchange velocity and the average residence time according to:

$$E = \left[\frac{\left|\log\left(\langle W\rangle_{\mathrm{HM}}\right) - \log\left(\langle W\rangle_{\mathrm{ASP,opt}}\right)\right|}{\log\left(\langle W\rangle_{\mathrm{ASP,opt}}\right)} + \frac{\left|\log\left(\langle T\rangle_{\mathrm{HM}}\right) - \log\left(\langle T\rangle_{\mathrm{ASP,opt}}\right)\right|}{\log\left(\langle T\rangle_{\mathrm{ASP,opt}}\right)}\right]. \tag{15}$$

The logarithms in Equation 15 were introduced to give an equal weight between the average residence time and the average exchange velocity. $\langle W\rangle_{\mathrm{HM}}$ and $\langle T\rangle_{\mathrm{HM}}$ were calculated using the HM model and the ranges of ε and n previously specified, while $\langle W\rangle_{\mathrm{ASP,opt}}$ and $\langle T\rangle_{\mathrm{ASP,opt}}$ were optimized from the tracer test using the ASP model. The parameter set ($\langle W\rangle_{\mathrm{HM},E_{\mathrm{min}}}$, $\langle T\rangle_{\mathrm{HM},E_{\mathrm{min}}}$, $\varepsilon_{E_{\mathrm{min}}}$, and $n_{E_{\mathrm{min}}}$), which is associated with the minimized error, E_{min}, was subsequently referred to as the optimized result of the HM model.

A visual comparison between the behavioral HEF parameter sets of the ASP model (Section 2.2.2); and the range of possible HEF parameters resulting from using the HM model with relevant choices of hyporheic zone depth and porosity (Section 2.3.5); was performed. We also compared the full residence time PDFs, that is, behavioral $f\left(T\right)_{\mathrm{ASP}}$ and possible $f\left(T\right)_{\mathrm{HM}}$, resulting from the behavioral range of $\langle T\rangle_{\mathrm{ASP}}$ and $\mathrm{CV}\left[T\right]_{\mathrm{ASP}}$ and possible range of $\langle T\rangle_{\mathrm{HM}}$ and $\mathrm{CV}\left[T\right]_{\mathrm{HM}}$, respectively. To illustrate the upper and lower boundaries of the behavioral $f\left(T\right)_{\mathrm{ASP}}$ we selected the maximum and minimum probability density of each residence time T. The same procedure was performed to illustrate the range of $f\left(T\right)_{\mathrm{HM}}$ resulting from different combinations of ε and n.

19447973, 2021, 12, Downloaded from https://agupubs.onlinelibrary.wiley.com/doi/10.1029/2021WR030248 by Statens Beredning, Wiley Online Library on [28/01/2024]. See the Terms and Conditions (https://onlinelibrary.wiley.com/terms-and-conditions) on Wiley Online Library for rules of use; OA articles are governed by the applicable Creative Commons License

Table 2
Parameters From the Tracer Test Assessment Including the Discharge at the Injection Point Q_0, Dispersion E, In-Stream Velocity U, Average Hyporheic Exchange Velocity $\langle W \rangle_{ASP}$, Average Residence Time $\langle T \rangle_{ASP}$, and the Coefficient of Variation $CV[T]_{ASP}$; and Average Independently Measured Stream Characteristics Including the Hydraulic Conductivity K, Stream Width w, Stream Depth d, Slope S, and Sinuosity s

	Tracer test assessment							Independent measurement				
	$Q_0\,(m^3/s)$	$E\,(m^2/s)$	$U\,(m/s)$	$\langle W \rangle_{ASP}\,(m/s)$	$\langle T \rangle_{ASP}\,(hr)$	$CV[T]_{ASP}\,(-)$	$\theta\,(-)$	$K\,(m/s)$	w (m)	$d\,(m)$	$S\,(-)$	$s\,(-)$
R1	0.012	0.41	0.164	4.18E-06	1.3	7.56E + 00	0	3.03E-04 ± 1.4E-04	1.9	0.12	2.44	1.41
R2a	0.005	0.12	0.044	6.66E-06	107	4.48E + 02	8.39E-04	3.36E-04 ± 8.0E-05	2	0.14	1.66	1.69
R2b	0.005	0.042	0.022	2.94E-07	7.9	1.70E-01	3.9E-09	3.37E-04 ± 1.17E-04	2.3	0.19	0.09	1.01
R3	0.005	0.066	0.018	9.08E-07	36.4	2.10E + 00	7.9E-06	3.55E-04 ± 1.6E-04	2.2	0.2	0. 12	1.04
R4	0.109	0.34	0.113	3.67E-05	0.7	1.18E + 02	2.7E-04	4.72E-04 ± 1.8E-04	6.3	0.45	0. 29	1.10
R6a	0.003	0.042	0.016	2.25E-06	11.9	2.60E + 01	4.7E-04	5.44E-04 ± 1.4E-04	2.7	0.18	0. 26	1.05
R6b	0.014	0.16	0.016	1.83E-06	40.7	3.41E + 01	0	5.76E-04 ± 1.9E-04	5.3	0.34	0.004	1.10
R6c[a]	0.065	0.06	0.072	2.58E-04	0.1	6.20E + 00	2.1E-08	5.13E-04[b] ± 1.5E-04	-	0.34	0. 43	1.03
R6d	0.099	0.04	0.087	6.00E-04	0.1	6.20E + 00	1.8E-04	6.86E-04[b] ± 5.6E-04	-	0.56	0. 08	1.01
R7	0.041	0.32	0.101	7.31E-06	25.4	2.40E + 02	1.8E-05	9.9E-04 ± 1.5E-04	2.7	0.18	0. 49	1.01

Note. For K, ±values represent the standard deviation of the measurements within in each reach.
[a]Reach R6c was optimized based on a single downstream BTC. [b]Hydraulic conductivity was measured in 2009 with the same device but by other researchers.

2.5. Generalizing Hyporheic Exchange at the Reach Scale

To generalize the insights that can be gained from cross-validating the two approaches, we used Buckingham's π theorm to define and teste a number of physical relationships between reach-averaged HEF parameters and hydraulic and geomorphological characteristics that can be measured in the stream. The purpose of applying this theorem is to identify the least number of independent, dimensionless parameters of the problem. The average exchange velocity normalized with the average hydraulic conductivity, $\frac{\langle W \rangle}{K}$, was selected as a fundamental dependent dimensionless parameter. By closely studying the integral that appears when Equation 13 is substituted into Equation 10, eight important, reach-averaged parameters $(K, \sigma_{y_b}, \sigma_{h_s}, g, U, d, \varepsilon, X)$ were identified (see the Text S4 in Supporting Information S1). From these eight parameters, we created seven dimensionless groups and statistically tested the following functional relationship:

$$\frac{\langle W \rangle}{K} = f\left(\frac{\sigma_{y_b}}{d}, \frac{\sigma_{h_s}}{d}, \frac{\sigma_{h_s}}{\sigma_{y_b}}, \frac{\varepsilon}{d}, \frac{U^2}{dg}, \frac{\sigma_{y_b}}{X}, \frac{\sigma_{h_s}}{X}\right) \tag{16}$$

where $\frac{U^2}{dg}$ is the squared Froude number. The importance of the independent parameter groups for the dimensionless average exchange velocity, and the agreement between models, was tested systematically by separately plotting $\frac{\langle W \rangle}{K}$ against the independent parameters.

3. Results

3.1. Field Experiments and Tracer Test Evaluation

The evaluation of the tracer test using the ASP model is visualized in Figure S6. All tracer tests were performed under low-flow conditions, and the discharges varied between 0.003 and 0.11 m^3/s among reaches (Table 2). Both stream depths and stream velocities were thus rather low, with the former varying between 0.12 and 0.56 m and the latter varying between 0.02 and 0.17 m/s. In general, the streams with high stream velocity also had comparably high dispersion. However, one exception was R6b, a meandering agricultural reach with low flow velocity that was densely vegetated at the time of the tracer test; where the dispersion was high, although the velocity was low.

19447973, 2021, 12, Downloaded from https://agupubs.onlinelibrary.wiley.com/doi/10.1029/2021WR030248 by Statens Beredning, Wiley Online Library on [28/01/2024]. See the Terms and Conditions (https://onlinelibrary.wiley.com/terms-and-conditions) on Wiley Online Library for rules of use; OA articles are governed by the applicable Creative Commons License

Magnitudes of optimized HEF parameters were within expected ranges, and among reaches, the average exchange velocity, $\langle W \rangle_{ASP}$, varied between 2.9E-07 and 6.0E-04 m/s, while the average residence time, $\langle T \rangle_{ASP}$, varied between approximately 0.1 and 100 h (Table 2). In streams with the largest discharges (R4, R6c, and R6d), exchange velocities were relatively high and residence times were relatively low compared to other reaches in both this study and previous studies (Morén et al., 2017; Riml et al., 2013; Wörman et al., 2002).

The performed MC-analysis focused on the parameters controlling the spread of the solute that is, $\langle W \rangle_{ASP}$, $\langle T \rangle_{ASP}$, $\mathrm{CV}\left[T\right]_{ASP}$, and E since the stream discharge and velocity was considered more sensitive. According to the MC analysis, the two most sensitive parameters of the four tested were E and $\langle W \rangle_{ASP}$, for which the dotty plots showed a distinct peak in most reaches (Figure S7 in Supporting Information S1). Compared to changes in E and $\langle W \rangle_{ASP}$, the model appeared less sensitive to changes in $\langle T \rangle_{ASP}$ and $\mathrm{CV}\left[T\right]_{ASP}$, resulting in large parameter ranges in the behavioral models (Figure S7 in Supporting Information S1). In particular, $\mathrm{CV}\left[T\right]_{ASP}$ could take almost any value within the investigated range in many of the reaches, while the optimization of $\langle T \rangle_{ASP}$ was mainly uncertain in reaches R3, R7, and R6b. In reaches R2b, R6c, and R6d, the range was relatively well constrained for both $\langle T \rangle_{ASP}$ and $\mathrm{CV}\left[T\right]_{ASP}$.

The independently measured hydraulic conductivity did not differ greatly among the reaches and ranged between 5.7E-05 and 9.9E-04 m/s, which corresponds to loam or sand. This result is in line with previous observations in streambeds using the method of falling head slug tests, both within the studied catchments (Morén et al., 2017; Riml et al., 2013) and in other regions (Stewardson et al., 2016; Ward & Packman, 2019).

3.2. Comparing the HM and ASP Model Results

After evaluating the key HEF parameters using the ASP model, the equivalent parameters were estimated (mostly) independently using the HM model. To compare the results, a sensitivity analysis was performed, evaluating the effect of the hyporheic zone depth and streambed porosity on the HM model results and the influence of these assumptions on the agreement with the ASP model results.

The flow-weighted average exchange velocity, $\langle W \rangle_{HM}$, is a Darcy velocity and thus independent on the streambed porosity. However, the sensitivity analysis showed that $\langle W \rangle_{HM}$ was largely dependent on the hyporheic zone depth ε. As the depth increased, $\langle W \rangle_{HM}$ increased, until it reached a plateau where the damping effect of the constrained hyporheic zone depth was negligible and the average hyporheic exchange velocity was conceived as being controlled by only the pressure variations at the streambed interface and the hydraulic conductivity of the sediments. In four of ten investigated reaches (R1, R3, R6b, and R7), this plateau occurred within the boundaries representing the behavioral values of $\langle W \rangle_{ASP}$ (Figure 1), indicating agreement between the two model approaches independently of the assumed hyporheic zone depth. In three reaches (R2a, R2b, and R6a), relatively shallow hyporheic zone depths were needed for $\langle W \rangle_{HM}$ to fall within the behavioral boundaries of $\langle W \rangle_{ASP}$. The hyporheic zone depth that corresponded to an exact agreement between $\langle W \rangle_{HM}$ and the optimized $\langle W \rangle_{ASP}$ varied between 0.03 and 0.25 m. In the three reaches with the largest stream discharges and cross-sectional areas, R4, R6c, and R6d, $\langle W \rangle_{HM}$ was considerably lower than $\langle W \rangle_{ASP}$, and an agreement between the two models was not possible by merely changing ε (Figure 1) or varying the average hydraulic conductivity within the confidence intervals.

The sensitivity analysis further shows that the average hyporheic residence time $\langle T \rangle_{HM}$ was relatively insensitive to geological changes, although a slight increase in $\langle T \rangle_{HM}$ with ε and n can be identified in some of the reaches (Figure S8 in Supporting Information S1). In general, these results indicate that changes in ε and n within the HM model did not control the agreement between the two models to a large extent. In four of the ten investigated reaches, R3, R6a, R6b, and R7, most combinations of ε and n resulted in $\langle T \rangle_{HM}$ within the boundaries of the behavioral $\langle T \rangle_{ASP}$, and in reach R2a, $\langle T \rangle_{HM}$ was slightly lower than the behavioral $\langle T \rangle_{ASP}$. However, in most reaches, $\langle T \rangle_{HM}$ was higher than the behavioral $\langle T \rangle_{ASP}$. In R4, R6c, and R6d, which were the largest reaches in terms of discharge and cross-sectional area, the difference was substantial, while in R1 and R2b, the ratio $\langle T \rangle_{HM}$ / $\langle T \rangle_{ASP}$ was less than 10.

To understand the causes of the observed differences between $\langle T \rangle_{HM}$ and the optimized $\langle T \rangle_{ASP}$, we also compared the full distribution of residence times, $f\left(T\right)_{HM}$ and $f\left(T\right)_{ASP}$. Figure 2 shows that $f\left(T\right)_{HM}$ and $f\left(T\right)_{ASP}$ partly agree but that deviations also exist in all reaches, mainly related to the largest values of T, which have the lowest probability densities but may have disproportional influences on the average values. In reaches, R4,

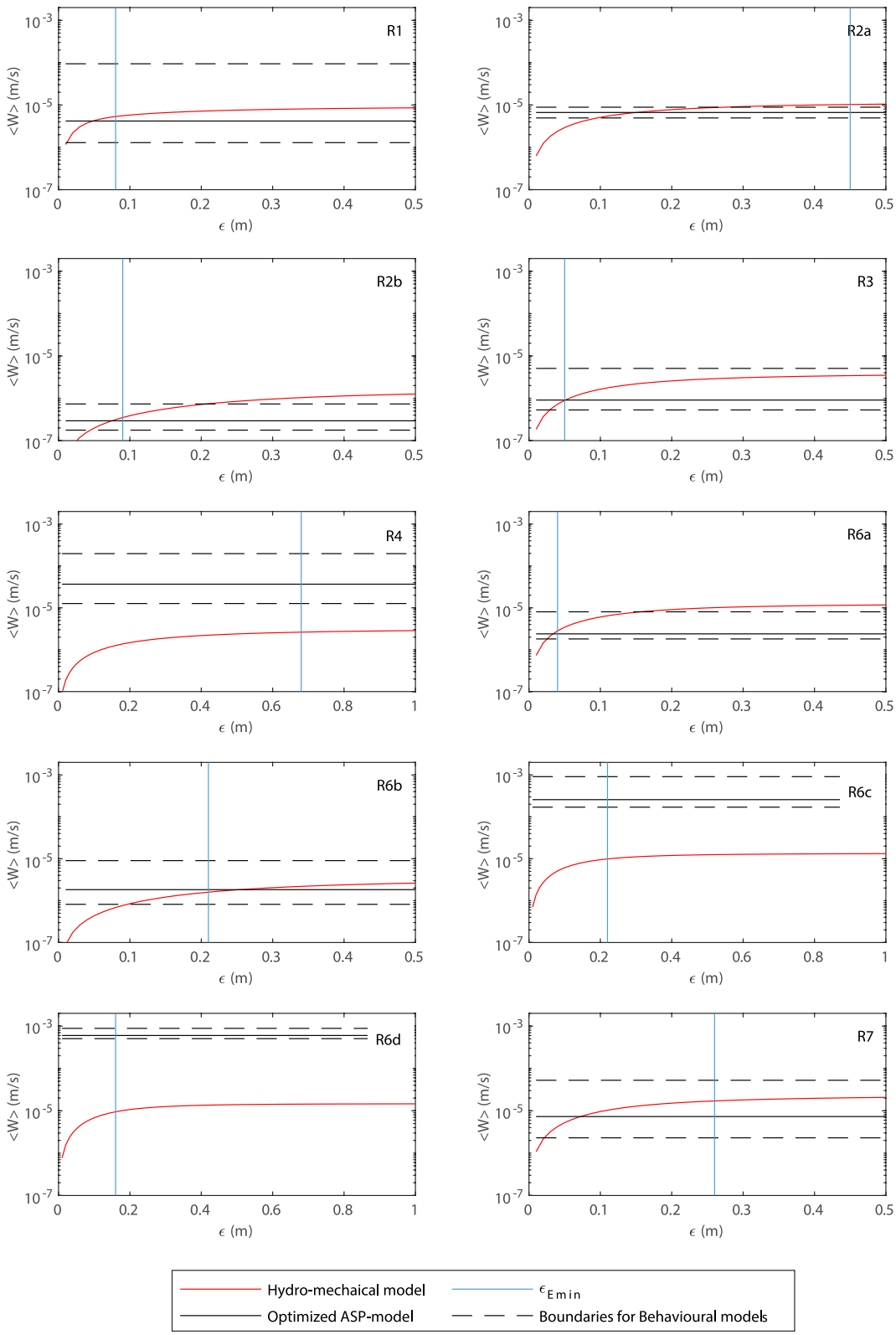

Figure 1. Flow weighted average hyporheic exchange velocity derived with the HM model ($\langle W \rangle_{\mathrm{HM}}$) as a function of hyporheic zone depth. Horizontal lines represent the optimized $\langle W \rangle_{\mathrm{ASP}}$ (black solid lines) and the boundaries of the $\langle W \rangle_{\mathrm{ASP}}$ considered behavioral (black dashed lines), which are independent from the hyporheic zone depth. The blue vertical lines represent the depth $\varepsilon_{E\mathrm{min}}$, leading to an optimal fit between the two models by minimization of the error defined by Equation 15.

19447973, 2021, 12, Downloaded from https://agupubs.onlinelibrary.wiley.com/doi/10.1029/2021WR030248 by Statens Beredning, Wiley Online Library on [28/01/2024]. See the Terms and Conditions (https://onlinelibrary.wiley.com/terms-and-conditions) on Wiley Online Library for rules of use; OA articles are governed by the applicable Creative Commons License

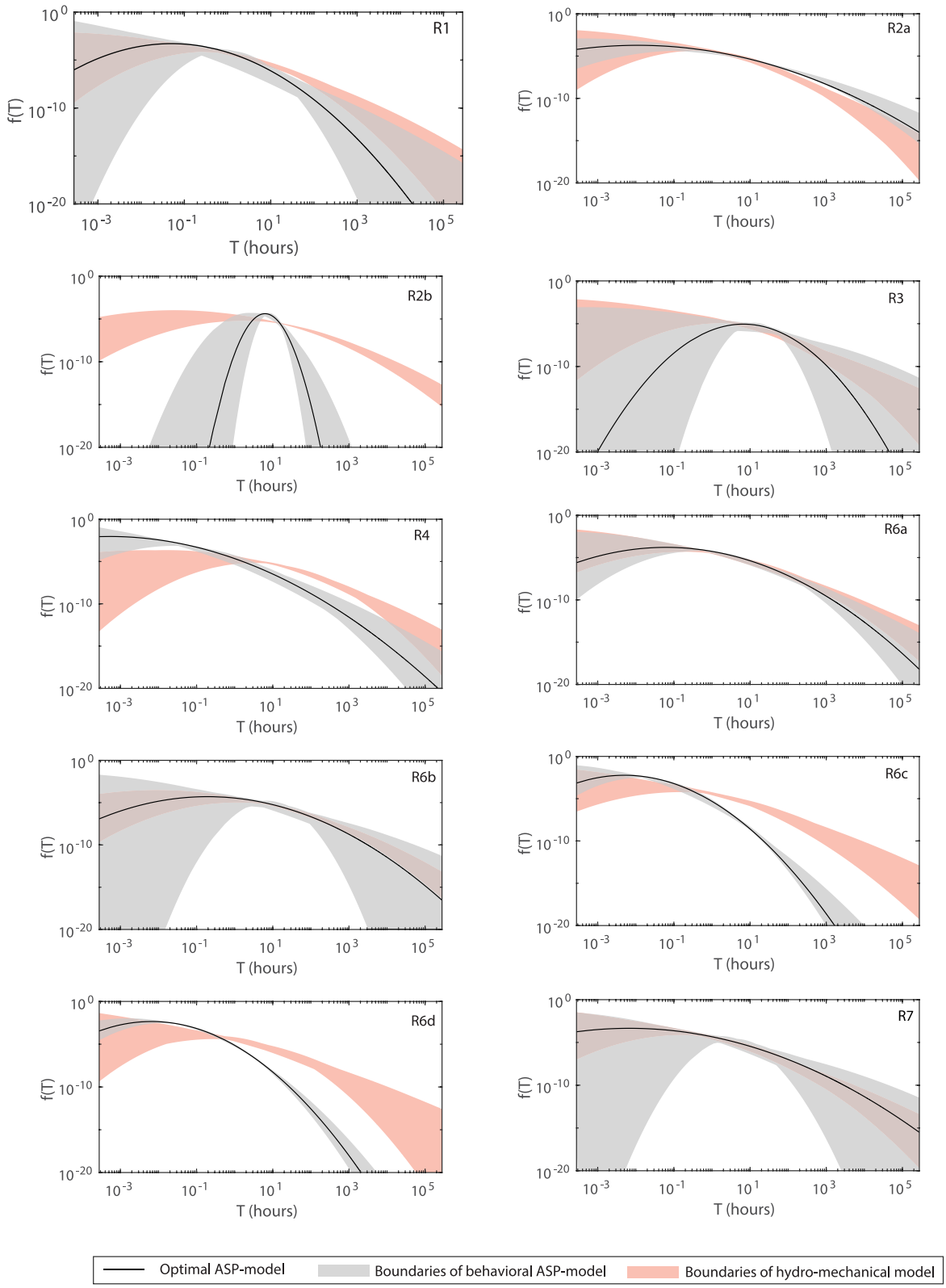

Figure 2. Hyporheic residence time PDFs derived with the ASP model supported by tracer data and the HM model supported by independent hydromorphologic data. The optimized ASP model (black solid line) is surrounded by a gray field that represents the maximum and minimum behavioral probability density for each residence time. The red field represents the maximum and minimum probability density derived with the HM model using a range of different porosities and hyporheic exchange depth.

19447973, 2021, 12, Downloaded from https://agupubs.onlinelibrary.wiley.com/doi/10.1029/2021WR030248 by Statens Beredning, Wiley Online Library on [28/01/2024]. See the Terms and Conditions (https://onlinelibrary.wiley.com/terms-and-conditions) on Wiley Online Library for rules of use; OA articles are governed by the applicable Creative Commons License

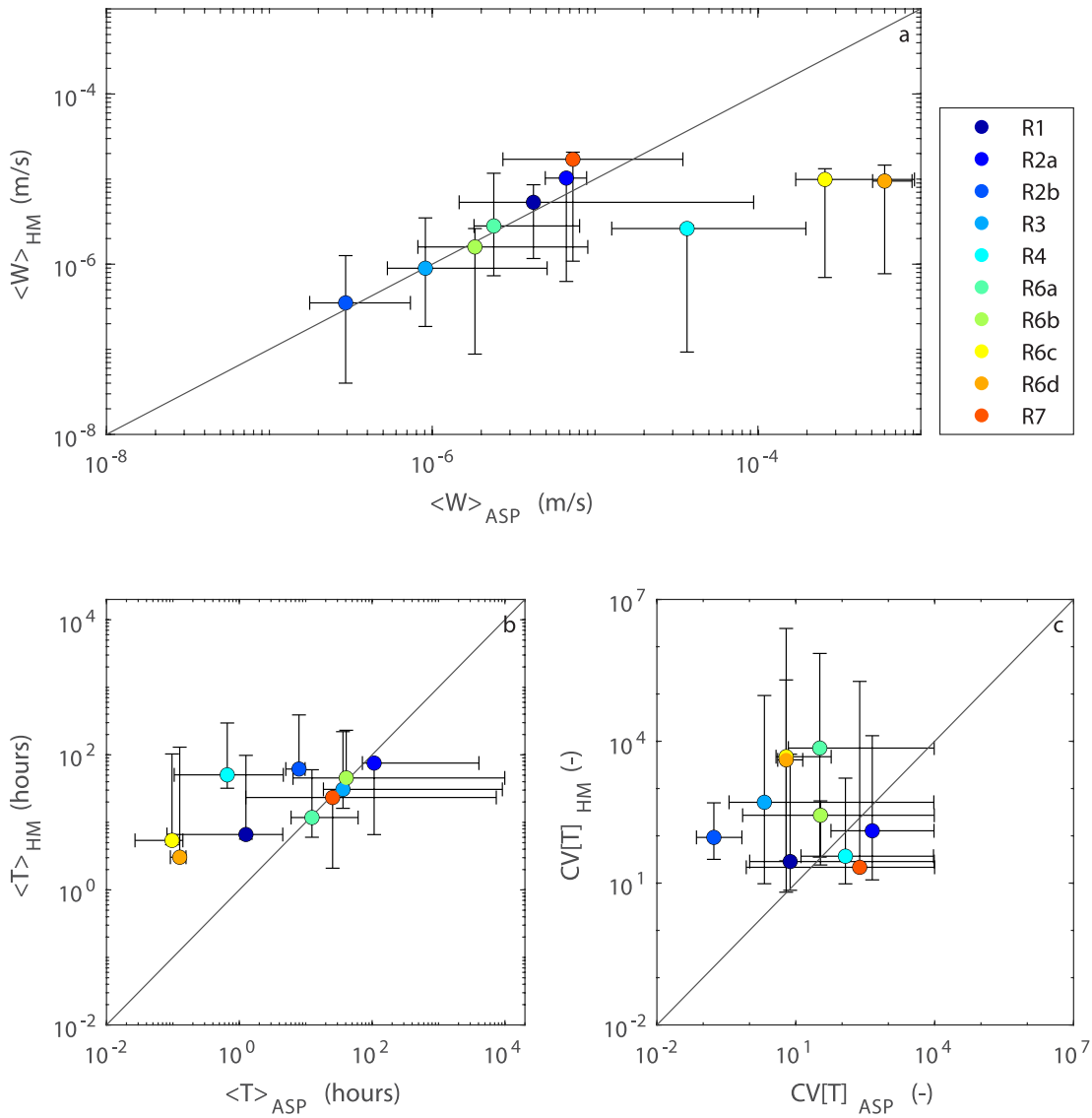

Figure 3. Comparison of the optimized ASP model and HM model in terms of (a) the average exchange velocity $\langle W \rangle$, (b) the average residence time $\langle T \rangle$ and (c) the coefficient of variation $\mathrm{CV}[T]$. The HM model was parameterized with independent measurements of streambed topography and hydraulic conductivity, and ε and n were chosen to minimize the combined error (Equation 15). Horizontal error bars represent behavioral parameters of the ASP model, and vertical error bars represent model sensitivity related to the hyporheic zone depth ε, which varies between 0.01 and 1 m, and the porosity n, which varies between 0.2 and 0.5.

R6c, and R6d, the whole distribution, $f(T)_{\mathrm{HM}}$, was slightly shifted to the right compared to $f(T)$ASP, that is, $\mu_{T,\mathrm{HM}} > \mu_{T,\mathrm{ASP}}$. In the rest of the reaches, the difference in the average residence time was explained by differences in the coefficient of variation, shown most clearly in R2b where all tested combinations of ε and n resulted in $f(T)_{\mathrm{HM}}$ much wider than the optimized and behavioral $f(T)_{\mathrm{ASP}}$ (Figure 2). Additionally, in reach R1, R3, R6a, and R6b $\mathrm{CV}[T]_{\mathrm{HM}}$ was larger than the optimized $\mathrm{CV}[T]_{\mathrm{ASP}}$ (Figure S9 in Supporting Information S1), but the evaluated $\mathrm{CV}[T]_{\mathrm{ASP}}$ was uncertain according to the MC analysis (Figure S7 in Supporting Information S1), resulting in behavioral $f(T)_{\mathrm{ASP}}$ that covers large intervals and overlapping red and gray fields in Figure 2.

The results of the cross-validation (Section 2.4) are illustrated in Figure 3, where the parameterization of the HM model that minimizes the combined error (i.e., $\langle W \rangle_{\mathrm{HM},E\mathrm{min}}$, $\langle T \rangle_{\mathrm{HM},E\mathrm{min}}$, and $\mathrm{CV}[T]_{\mathrm{HM},E\mathrm{min}}$, calculated using hyporheic zone depth $\varepsilon_{E\mathrm{min}}$ and porosity $n_{E\mathrm{min}}$) is plotted against parameters of the optimized ASP model. The two models showed agreement in terms of the average exchange velocity (Figure 3a), increasing the confidence that the presented values are relevant quantifications of the transversal flux across the streambed. More uncertainty

19447973, 2021, 12, Downloaded from https://agupubs.onlinelibrary.wiley.com/doi/10.1029/2021WR030248 by Statens Beredning, Wiley Online Library on [28/01/2024]. See the Terms and Conditions (https://onlinelibrary.wiley.com/terms-and-conditions) on Wiley Online Library for rules of use; OA articles are governed by the applicable Creative Commons License

19447973, 2021, 12, Downloaded from https://agupubs.onlinelibrary.wiley.com/doi/10.1029/2021WR030248 by Statens Beredning, Wiley Online Library on [28/01/2024]. See the Terms and Conditions (https://onlinelibrary.wiley.com/terms-and-conditions) on Wiley Online Library for rules of use; OA articles are governed by the applicable Creative Commons License

was however related to the distribution of residence times, as indicated by the discrepancies shown in Figures 3b and 3c. Furthermore, Figure 3 illustrates the smaller range of values resulting from the HM model compared to the ASP model, that is, that the largest $\langle W \rangle_{\mathrm{ASP}}$ and the smallest $\langle T \rangle_{\mathrm{ASP}}$ and $\mathrm{CV}\left[T\right]_{\mathrm{ASP}}$ were not captured by the HM model. The two models showed the best agreement in R3, R6a, R7, and R2b, where E_{min}, in general, was low compared to that in the other reaches. However, even in these reaches, there was a large deviation in the coefficient of variation. E_{min} was largest in reaches R4, R6c, and R6d, which were the largest reaches in terms of both discharge and average cross-sectional area.

3.3. Hyporheic Exchange Mechanisms and Scale Dependency

We utilized the HM model presented here to investigate the spectral distribution of HEF and to decompose the static and dynamic head drivers of the flow into different spatial scales. Furthermore, we tested how extrapolation of the topography and hydraulic head spectra to wavelengths of 1 cm affected the relative importance of static head-driven exchange versus dynamic head-driven exchange and to determine if it could improve the agreement between the two tested approaches.

The results show that the exchange spectrum $S_W\left(\lambda\right)$ (Equation 13), which reflects the HEF as a function of wavelength, was curve-shaped with maximum values at wavelengths between 0.2 and 3.2 m (Figure 4). The exchange spectra further show that the static head-driven hyporheic exchange velocity was much higher than the dynamic head-driven velocity across all observed spatial scales (Figure 4). However, when the spectra were extrapolated to non-observed spatial scales, the dynamic and static exchange spectra intersects in some of the reaches, which indicates that the dynamic head-driven hyporheic exchange velocity could be dominant at scales smaller than approximately 10 cm.

The effect that small topographical scales can have on the average exchange velocity was tested by integrating the spectra according to Equation 10 using (a) an increased upper cutoff, λ_{max} (Figure 5a), and (b) a decreased lower cutoff λ_{min} (Figures 5b and 5c). This analysis showed that small scales dominated the exchange. When λ_{min} was set to 1 cm and the effect of the upper wavelength limit λ_{max} was analyzed, features with wavelengths smaller than five meters accounted for more than 90% of the total $\langle W \rangle_{\mathrm{HM}}$. The result can be observed in Figure 5a as the constant value of $\langle W \rangle_{\mathrm{HM}}$ that was found in all reaches at $\lambda_{\mathrm{max}} = 5$ m (and in most reaches at even lower λ_{max}), indicating that the inclusion of additional larger spatial scales (i.e., larger wavelengths) did not contribute significantly to the exchange velocity. In contrast, when λ_{min} was evaluated, the analysis showed that $\langle W \rangle_{\mathrm{HM}}$ increased when smaller scales were included compared to the measured value, but it also reached a plateau relatively fast at a wavelength of approximately 10 cm in most reaches (Figure 5b). This indicates that features of length 10 cm or shorter have little impact on the average exchange velocity and that observed spatial scales were sufficient to evaluate $\langle W \rangle$. Furthermore, this finding indicates that in the reaches where an agreement between the two models was not possible (R4, R6c, and R6d), the increase in $\langle W \rangle_{\mathrm{HM}}$ from the inclusion of smaller spatial scales did not overcome the deviation; and in most of the reaches where $\langle W \rangle_{\mathrm{HM}}$ and $\langle W \rangle_{\mathrm{ASP}}$ agreed, $\langle W \rangle_{\mathrm{HM}}$ remained within the boundaries of the behavioral $\langle W \rangle_{\mathrm{ASP}}$ even when smaller spatial scales were included (Figure S10 in Supporting Information S1). However, in reach R6b and R2b, $\langle W \rangle_{\mathrm{HM}}$ increased by a factor of approximately 8 and 5, respectively, when including scales down to 1 cm, which yielded a $\langle W \rangle_{\mathrm{HM}}$ that was slightly higher than the behavioral $\langle W \rangle_{\mathrm{ASP}}$. Furthermore, in reach R1, $\langle W \rangle_{\mathrm{HM}}$ also increased by a factor of approximately 5, but remained within the boundaries of the behavioral $\langle W \rangle_{\mathrm{ASP}}$, which were relatively wide.

When using the observed streambed topography to calculate $\langle W \rangle_d$ and $\langle W \rangle_s$, the ratio between them was below one in all reaches, indicating that static head exchange was dominant. The relative contribution of the dynamic head fluctuations did increase when λ_{min} was decreased, highlighting a higher relative importance of dynamic head variations for hyporheic exchange velocities as smaller spatial scales were included. However, $\langle W \rangle_d$ / $\langle W \rangle_s$ only exceeded one in two of the reaches (R6a and R2b), indicating a dominance of static head-driven hyporheic exchange in the majority of the reaches regardless of the limiting lower wavelength (Figure 5c). In reaches R6a and R2b, a dominance of the dynamically driven HEF was found when including wavelengths smaller than 5 and 2 cm, respectively.

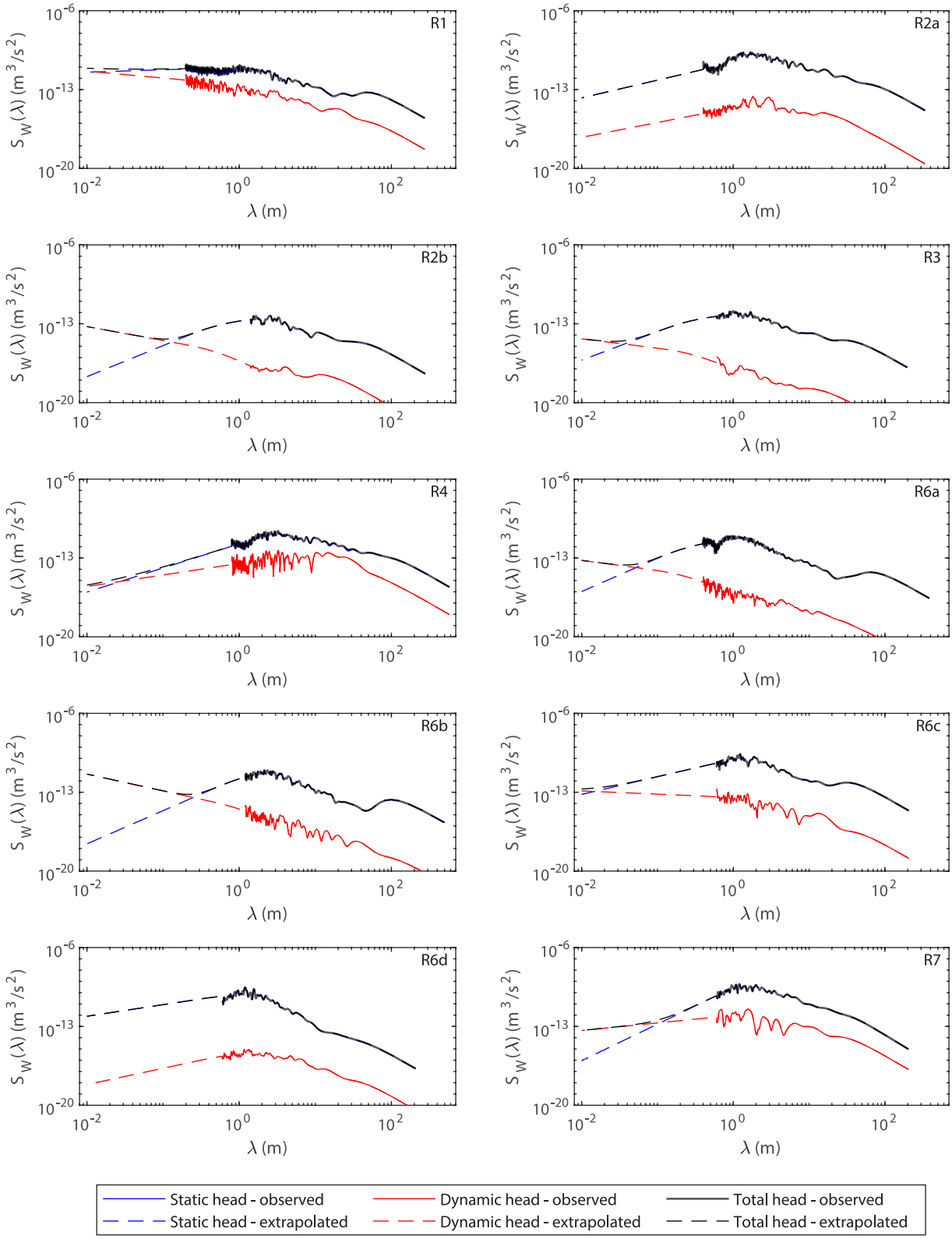

Figure 4. Estimated dynamic, static, and total exchange spectra based on observed data only (solid lines) and extrapolated to a wavelength of 1 cm (dashed lines). Note that the blue curve is hidden under the black for the main part of the larger wavelengths.

19447973, 2021, 12, Downloaded from https://agupubs.onlinelibrary.wiley.com/doi/10.1029/2021WR030248 by Statens Beredning, Wiley Online Library on [28/01/2024]. See the Terms and Conditions (https://onlinelibrary.wiley.com/terms-and-conditions) on Wiley Online Library for rules of use; OA articles are governed by the applicable Creative Commons License

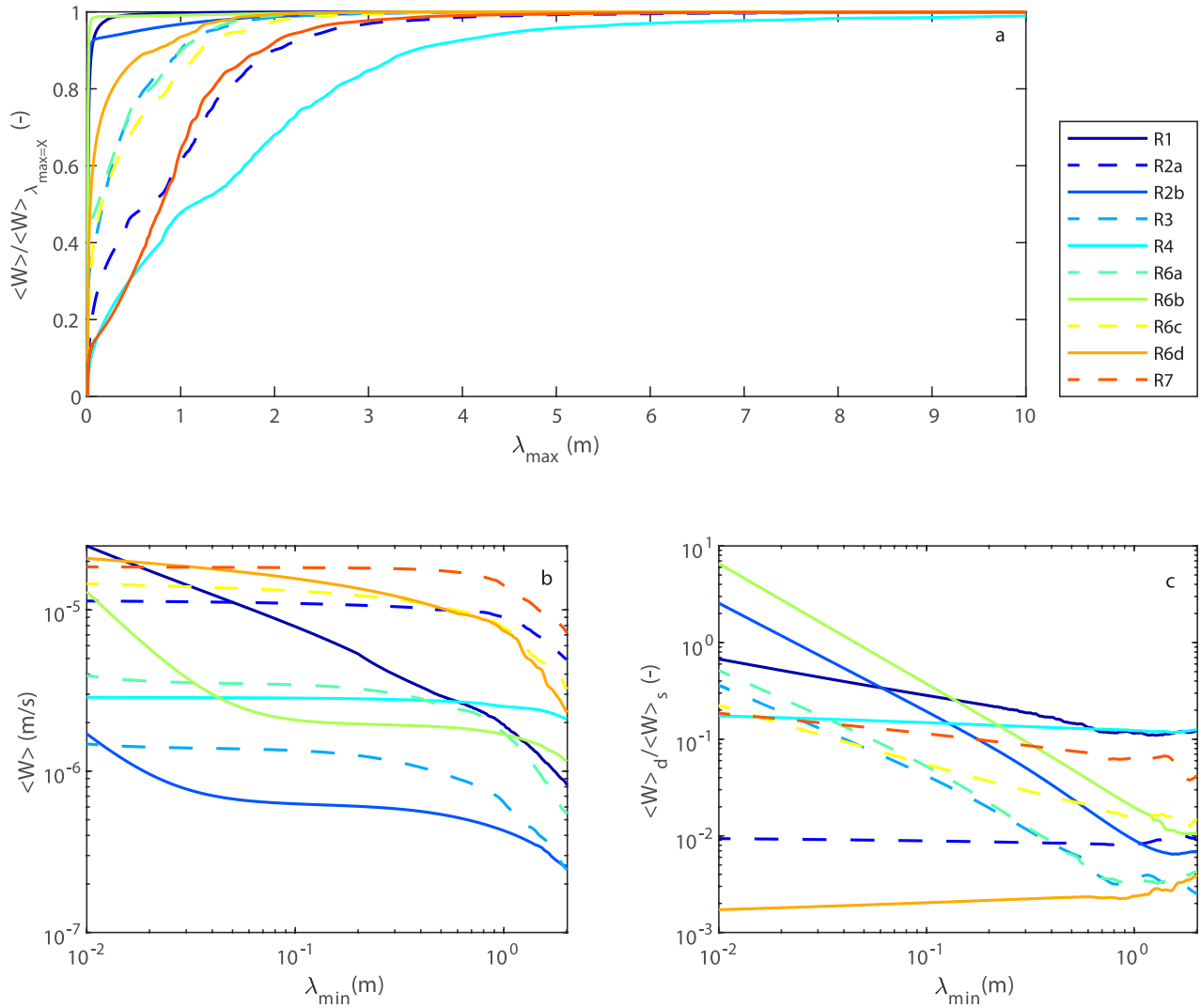

Figure 5. Flow weighted average exchange velocity as a function of different wavelength cutoffs in the exchange spectrum, for all reaches. Specifically, (a) the effect of maximum wavelength λ_{max} on the exchange velocity relative to the maximum exchange velocity $\langle W \rangle_{HM,\lambda_{max}=X}$; (b) the effect of the exchange spectrum minimum wavelength λ_{min} on the total average exchange velocity and (c) the ratio between dynamic head-driven exchange and static head driven exchange.

4. Discussion

In this study, we employed two considerably different approaches to quantify the HEF in 10 stream reaches with varying characteristics. Both approaches expressed the advective component of hyporheic flow along a distribution of streamlines within the stream bed but the ASP model induced parameters from a tracer test; while the HM model deducted HEF-parameters from independent measurements of the streambed topography and WSP along the stream thalweg. Our results showed that the two approaches could be cross-validated in most investigated streams, in terms of the average hyporheic exchange velocity, while more variation was observed when the residence time PDFs were compared. The cross-validation indicates that HEF is mainly driven by head variations along the streambed interface that are created by hydrodynamic effects or gradient variations in the WSP. This finding supports previous studies that have interpreted results from the ASP model or other similar phenomenological models as estimates of physical quantities such as the transversal flux across the streambed and average residence times within it.

19447973, 2021, 12, Downloaded from https://agupubs.onlinelibrary.wiley.com/doi/10.1029/2021WR030248 by Statens Beredning, Wiley Online Library on [28/01/2024]. See the Terms and Conditions (https://onlinelibrary.wiley.com/terms-and-conditions) on Wiley Online Library for rules of use; OA articles are governed by the applicable Creative Commons License

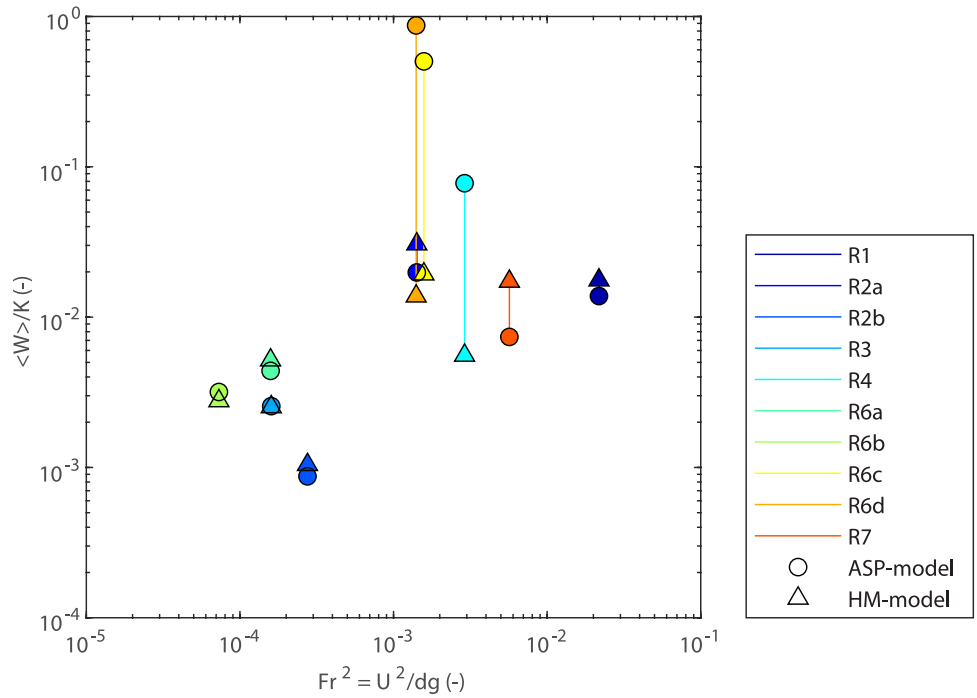

Figure 6. Dimensionless average exchange velocity $<W>/K$ derived with the ASP model and HM model as a function of the Froude number. Vertical lines between triangles and circles indicate that the two markers represent the same reach. Reaches are also marked with different colors according to the legend.

4.1. Geomorphological and Hydraulic Parameters Controlling Reach-Scale HEF

The cross-validation of the two models supports the generalization of the relationships between the dimensionless average exchange velocity $\langle W \rangle / K$ (dependent parameter) and seven (independent) dimensionless parameters appearing in the HM model, that is, $\frac{\sigma_{y_b}}{d}, \frac{\sigma_{h_s}}{d}, \frac{\sigma_{h_s}}{\sigma_{y_b}}, \frac{\varepsilon}{d}, Fr, \frac{\sigma_{y_b}}{X}$, and $\frac{\sigma_{h_s}}{X}$ (Section 2.5). In this section, we mainly discuss the relationship with the Froude number, which we consider the strongest of the investigated cases, while the full results are presented in the Supporting Information (Figure S11 in Supporting Information S1). We observed a general increase in $\frac{\langle W \rangle_{\mathrm{HM}}}{K}$ with Fr^2 (Figure 6), which agrees with previous research (Sawyer et al., 2011; Wörman et al., 2002). This finding reflects the impact of drag over bed forms, as mathematically described in Equation 6, but can also be related to factors controlling the variations in the WSP, as discussed in for example, Mojarrad et al. (2019) and Sawyer et al. (2011). According to the theory of open channel hydraulics, the gradient in the WSP over a short distance depends on the Froude number according to $\left(\partial\left(y_b + d\right) / \partial x\right) / \left(\partial y_b / \partial x\right) = 1 + 1 / \left(Fr^2 - 1\right)$, implying that the static head conversion factor increase with an increase in Fr^2 in subcritical flow conditions and decreases with an increase in Fr^2 in supercritical flow conditions. Since we detected subcritical conditions in all investigated streams, it is possible that both static head gradients and dynamic head gradients, which both increase with Fr^2, are responsible for the relationship observed in Figure 6.

From studying the other relationships in Figure S11 in Supporting Information S1, we noticed a positive correlation between the dimensionless average exchange velocity and the standard deviation of the detrended stream bottom and WSP, regardless of whether it was normalized with stream depth or stream length. However, this trend was not observed for the reaches with the worst agreement between the two modeling approaches (reaches R4, R6c, and R6d). Since low $\frac{\sigma_{h_s}}{d}$ is an indicator of high relative submergence of bed forms, this result implies only slight variations in the WSP in these reaches and a potential for dynamic head gradients to dominate as drivers of HEF. However, the observed uncertainty in the relationships shows that the normalized standard deviation cannot alone represent the topographical variations and explain the variability in $\langle W \rangle$/K between reaches and that the

19447973, 2021, 12, Downloaded from https://agupubs.onlinelibrary.wiley.com/doi/10.1029/2021WR030248 by Statens Beredning, Wiley Online Library on [28/01/2024]. See the Terms and Conditions (https://onlinelibrary.wiley.com/terms-and-conditions) on Wiley Online Library for rules of use; OA articles are governed by the applicable Creative Commons License

19447973, 2021, 12, Downloaded from https://agupubs.onlinelibrary.wiley.com/doi/10.1029/2021WR030248 by Statens Beredning, Wiley Online Library on [28/01/2024]. See the Terms and Conditions (https://onlinelibrary.wiley.com/terms-and-conditions) on Wiley Online Library for rules of use; OA articles are governed by the applicable Creative Commons License

distribution of head gradients along the streambed and across different wavelengths (included in the HM model) is also important to consider to exactly quantify the average hyporheic exchange velocity. Nevertheless, the identified links between $\langle W \rangle$ / K and reach-averaged dimensionless characteristics can be utilized as the first indicator of HEF or to reduce uncertainty when evaluating HEF using transport models to interpret tracer tests. However, first, a larger data set than the 10 reaches investigated here and that is extracted from an even wider range of hydro geomorphologic conditions is needed to more generally establish the relationships.

4.2. Processes Induced From Tracer Tests That Are Not Represented by the HM Model

This study showed that the two models could be cross-validated in terms of the average exchange velocity, but that uncertainties existed, mainly related to the residence time PDFs in the hyporheic zone. An explanation of these uncertainties is that we here interpreted all retention of the tracer BTC as HEF driven by head fluctuations at the streambed interface (pumping), while in reality the retention might be caused by other processes, that are not represented by the HM model.

One such mechanism is turbulent diffusion, which mainly occurs in the upper part of the sediment and results in short timescales and fast exchange velocities. It can be important both in flat bed streams, where it is assumed to dominate the HEF, and in highly permeable beds with bed forms, where it may further enhance the exchange velocity (e.g., Grant et al., 2018; Packman et al., 2004). The exclusion of this mechanism from the HM model may explain the lower $\langle W \rangle_{\mathrm{HM}}$ compared to $\langle W \rangle_{\mathrm{ASP}}$ and higher $\langle T \rangle_{\mathrm{HM}}$ compared to $\langle T \rangle_{\mathrm{ASP}}$ in reaches R4, R6c, and R6d. This theory is strengthened by the fact that these three reaches have the highest Reynolds numbers, defined as $\mathrm{Re} = Ud / \nu$, where ν (m^2/s) is the kinematic viscosity (Figure S12 in Supporting Information S1). A high Re indicates a high turbulent diffusion coefficient, which is used to quantify turbulent diffusion across the streambed interface (e.g., Packman et al., 2004). However, the generally positive relationship between Re and $\langle W \rangle_{\mathrm{HM}}$ / K, which has been observed previously by Grant et al. (2018) and Packman et al. (2004), could also reflect highly dynamic head-driven exchange due to its proportionality to U (Equation 6). Considering the characteristics of the streambed sediment, turbulence could be important in R6c and R4, where the streambed sediment consisted of washed-out gravel and stones in the steeper parts of the reaches, but was less likely in reach R6d, where sediments were more clayey.

Another alternative mechanism that could explain the fact that $\langle W \rangle_{\mathrm{HM}}$ was lower than $\langle W \rangle_{\mathrm{ASP}}$ and that $\langle T \rangle_{\mathrm{HM}}$ was higher than $\langle T \rangle_{\mathrm{ASP}}$, in the three reaches R4, R6c and R6d could be the exchange with stagnant surface water. This retention mechanism can have significant effects on tracer BTCs in streams with low gradients, dense in-stream vegetation and deep water (Briggs et al., 2009; Johnson et al., 2014), similar to the conditions observed in reach R6d. In addition, lateral hyporheic flow, for example flow through stream meanders, is a mechanism that was not accounted for by the two-dimensional HM model. This could explain the high residence times in reach R2a, concluded by the ASP model, since this reach was among the steepest reaches and had the highest sinuosity of 1.69 (Table 2), which provides potentially long flow paths through meander bars.

4.3. Uncertainty in the Cross-Validation of the Residence Time Distribution

When comparing the entire RTDs derived with the two models, the results indicated that although the mean values of the distributions showed agreement, the variance in the distributions varied substantially. This variation was manifested as large differences between $\mathrm{CV}\left[T\right]_{\mathrm{HM}}$ and $\mathrm{CV}\left[T\right]_{\mathrm{ASP}}$ and, in some cases, between $\langle T \rangle_{\mathrm{HM}}$ and $\langle T \rangle_{\mathrm{ASP}}$.

These uncertainties could be related to uncertainties in the data and the evaluation of the two models, such as the estimation of $\langle T \rangle_{\mathrm{ASP}}$ and $\mathrm{CV}\left[T\right]_{\mathrm{ASP}}$, which was uncertain according to the MC-analysis. There is a statistical relationship between the average residence time and the variance in a log-normal PDF (Wörman & Wachniew, 2007), which can cause equifinality in the model optimization toward the tracer BTC, thus several different pairs $\left[\langle T \rangle_{\mathrm{ASP}}, \mathrm{CV}\left[T\right]_{\mathrm{ASP}}\right]$, that lead to exactly the same model fit. Furthermore, due to its documented adsorptive characteristics (Runkel, 2015), the use of RWT as a conservative tracer to estimate HEF variables is a source of uncertainty for the ASP model results. However, the mass conservation between the sampling points was never below 72%, and was only below 100% in three of the reaches, indicating that adsorption has a minor impact on the transport of RWT in the streams investigated here (Table S1 in Supporting Information S1). The observed

19447973, 2021, 12, Downloaded from https://agupubs.onlinelibrary.wiley.com/doi/10.1029/2021WR030248 by Statens Beredning, Wiley Online Library on [28/01/2024]. See the Terms and Conditions (https://onlinelibrary.wiley.com/terms-and-conditions) on Wiley Online Library for rules of use; OA articles are governed by the applicable Creative Commons License

mass loss was explained in the ASP model as dilution, which is reasonable given that the three reaches with the lowest mass recovery (R2a, R6a, and R4) were among the steepest reaches, and could thus be expected to receive relatively high fluxes of upwelling groundwater. However, a sensitivity analysis of the impact of reversible and irreversible sorption on the ASP model variables showed that reversible sorption, or relatively low levels of irreversible sorption, might exist in reach R2b, and possibly in the other reaches. However, adsorption had relatively small impact on the other model variables when accounted for in the ASP model and would therefore not change the general results of the study (Text S3, Table S2 in Supporting Information S1).

Uncertainty in the cross-validation can also be related to uncertainties in how the residence time PDFs were defined in the HM model, that is, in the particle tracking routine that did not account for variations in the hydraulic conductivity within the streambed. Including the heterogeneity of streambed sediment in models for HEF can cause both increasing and decreasing residence times (compared to homogenous sediments) depending on the relative positions of the heterogeneities (Cardenas & Wilson, 2004). Furthermore, the upper boundary condition of the MH model was defined from the topography PSD, which describes only the main characteristics of the hydraulic head patterns along the reaches. Studies have shown that the longest hyporheic flow paths, which are often related to the longest residence times, start at a few specific locations along the streambed where head gradients induced by features of different sizes reinforce each other (Herzog et al., 2019). In the HM model, the longest flow paths were directly related to the longest PSD wavelength (i.e., steam length), and the random interactions between features of different wavelengths were not accounted for.

Nevertheless, in some reaches, even the wide range of residence time PDFs considered behavioral according to the ASP model did not agree with those obtained with the HM model, indicating that conceptual differences between the two models also contributed to the disagreement and that different model frameworks emphasize different parts of the residence time PDF in the hyporheic zone. Tracer test BTCs reflect the part of the solute that returns to the stream within the observed reach length and observation time period, and the subsequent assessment is highly affected by instrumental detection limits (Bencala et al., 2011) and truncation of the BTC tail (Drummond et al., 2012). As a result, the longer time scales of the residence time PDF are often omitted, which might lead to residence times that are controlled mainly by the length of the stream reach, advective travel time (X / U) or window of detection, that is, time from the first arrival to last detection of the tracer (Gooseff et al., 2013; Harvey & Wagner, 2000; Schmadel et al., 2016). In this study, the reaches with the lowest X / U (R6c and R6d) had the lowest evaluated $\langle T \rangle_{\mathrm{ASP}}$ and the largest differences between the ASP model and HM model in terms of both residence time and exchange velocity. The generally wider RTDs provided by the HM model compared to the ASP model could thus be explained by limitations in the window of detection.

In contrast to solute transport models accounting for HEF, physically based models tend to capture higher residence times because they are limited by their resolution. In a multiscale model, such as the HM model presented here, the resolution is represented by the ranges of wavelengths in the PSDs, which are limited by the resolutions of the measured topography and WSP. We tested the effect of including smaller scales than those measured by extrapolating the stream bottom elevation PSD, which resulted in a slightly higher average exchange velocity, indicating a slightly lower average residence time and thus better agreement with the ASP model results.

4.4. Impacts of Different Spatial Scales on the Average Exchange Velocity

In addition to cross-validating the two models, another objective of this study was to use the HM model to examine the relative importance of different spatial scales for the HEF in the different reaches. The results indicate that more than 90% of the hyporheic exchange was accounted for in the HM model even when wavelengths larger than 5 m were excluded. This was true for all reaches and agrees with previous studies showing that flow-induced by small-scale features dominates the HEF (Gomez-Velez & Harvey, 2014; Stonedahl et al., 2012, 2013; Wörman et al., 2006). These small scales correspond to geomorphological features such as bed forms or obstacles in the form of wooden debris and boulders, with lengths of decimeters to several meters. The result reflects that the distribution of HEF across different wavelengths was largely controlled by the depth of the hyporheic zone, which dampens the velocity along flow paths associated with $\lambda > \varepsilon$, through the geological damping factor (Equation 9). For the analysis, we used values of $\varepsilon_{E\mathrm{min}}$ that led to optimal agreement between the HM model and the ASP model and varied between 0.04 and 0.68 m among reaches.

19447973, 2021, 12, Downloaded from https://agupubs.onlinelibrary.wiley.com/doi/10.1029/2021WR030248 by Statens Beredning, Wiley Online Library on [28/01/2024]. See the Terms and Conditions (https://onlinelibrary.wiley.com/terms-and-conditions) on Wiley Online Library for rules of use; OA articles are governed by the applicable Creative Commons License

The dominance of HEF driven by head gradients over small features highlights the importance of high-density and high-quality topographical input data when modeling HEF using a deductive model such as the HM model presented here. Since HEF is driven by head gradients, that is, an elevation difference over a distance, small uncertainties in topographical input data can have a large impact on the result. In general, we estimated an error of ±2 mm in the bottom elevation measurements and an error of ±7 mm in the WSP measurements. This error could be problematic considering that the total elevation drop along the entire length of the reach, that is, SX, which restricts the possible variation in the WSP, was lower than 1 m in several reaches and as low as 2 cm in R6b, which had the lowest slope. When analyzing the three spectra employed as input in the HM model, we discovered possible measurement errors. As expected, the streambed elevation PSDs, S_{y_b}, generally had higher magnitudes than the surface water profile PSDs, S_{h_s}, reflecting higher variations in the streambed elevation compared to the WSP. However, an unexpected increase in the static conversion factor, defined as $\gamma_{h_s} = S_{h_s} / S_{y_b}$, above one was observed at scales smaller than a few centimeters (Figure S13 in Supporting Information S1). This finding indicates that over these very short wavelengths, certain variations in the WSP exceeded those in the streambed. Whether these results reflect measurement errors, problems related to the extrapolation of the PSDs, or real gradients in the WSP is difficult to conclude with certainty. However, the results conclude that the utilization of emerging new methods for the collection of high-resolution topography data (Passalacqua et al., 2015; Woodget et al., 2017) would improve the certainty of the HM model. This utilization would also simplify the field measurements and motivate the use of the HM model or a similar multiscale model for parameterization of solute transport models traditionally parameterized through calibration against tracer tests.

4.5. The Relative Importance of Static and Dynamic Exchange

When the originally measured topography and WSP were employed, our results indicate a dominance of static head-driven HEF in all reaches, independent of slope and discharge. The general dominance of static head fluctuations over dynamic head fluctuations as drivers of HEF has been observed previously in mountainous catchments (Marzadri et al., 2014; Mojarrad et al., 2019). In addition, measurements of static and dynamic head in a flume with riffle-pool characteristics showed general dominance of static head gradients; but also observed that the dynamic head gradients were allowed to dominate the HEF in deeper areas, where the overlying water surface was flat (Tonina & Buffington, 2007). One reason for the general dominance of the static head observed here could thus be the included spatial scales, that is, wavelengths in the HM model. Studies that reached the opposite conclusion, that is, that the dynamic head gradients dominated as drivers of hyporheic exchange over longer stream reaches, assumed that no static head gradients (except the average slope) existed across wavelengths smaller than a certain size (Gomez-Velez & Harvey, 2014; Stonedahl et al., 2012, 2013).

Some studies suggest that HEF is mainly driven by static gradients in high-order reaches, which are generally steep, have low discharge and exhibit low relative submergence of bed forms, but that dynamic head gradients successively take over the control of HEF when moving toward lower stream order reaches with lower slopes and higher discharges (Wondzell et al., 2019). In this study, the inclusion of smaller wavelengths in the hydraulic head PSD increased the $\langle W \rangle_d / \langle W \rangle_s$ ratio, but it was consistently smaller than one in all reaches except for reach R6b and R2b. According to the abovementioned theory by Wondzell et al. (2019), this result is probably attributed to the low slopes of reaches R6b and R2b, which produce static head gradients that are considerably restricted; thus, a HEF that is mainly driven by head gradients created when stream flow interacts with small, submerged, bed forms and riffles. Once again, we notice that measurement errors might cause an overestimation of the static head gradients across the shortest wavelength and thus an underestimation of $\langle W \rangle_d / \langle W \rangle_s$. Note also that this ratio depends on Equation 6, which was originally developed empirically to explain the hydrodynamic head over triangular bed forms with an overlying flat water surface and constant hydraulic regime (Elliott & Brooks, 1997a, 1997b). Subsequently, the equation has been extended to account for the variations in stream depth and velocity along the reach and for more complex stream geomorphologies (Stonedahl et al., 2010). Although this formulation and other similar formulations have been employed in several studies (Marzadri et al., 2014; Mojarrad et al., 2019; Morén et al., 2017; Stonedahl et al., 2012; Wörman et al., 2006), they have, to our knowledge, not been validated against independent measurements, and might not be suitable after harmonics have been superimposed. If this is the case, it might also explain the discrepancy between the HM model results and the ASP model results in streams with high velocities and large relative submergence, where dynamic head fluctuations are most likely significant. Additional studies of the relationship are needed to be able to more correctly formulate the multiscale

19447973, 2021, 12, Downloaded from https://agupubs.onlinelibrary.wiley.com/doi/10.1029/2021WR030248 by Statens Beredning, Wiley Online Library on [28/01/2024]. See the Terms and Conditions (https://onlinelibrary.wiley.com/terms-and-conditions) on Wiley Online Library for rules of use; OA articles are governed by the applicable Creative Commons License

variations in hydraulic head gradients at the streambed and consequently improve cross-validations of the type presented in this study.

5. Conclusion

In this study, we investigated if two considerably different approaches for quantifying reach-averaged HEF could be cross-validated and showed that this case applied for the average exchange velocity but that more uncertainty was related to the cross-validation of the RTD. The results indicate that the presented multiscale HM model supported with independent hydromorphological data offers a physical explanation for the average exchange velocity obtained from stream tracer test assessments, in small alluvial streams, with low discharge, shallow depth, and moderate slope. In particular, this cross-validation was consistent with previous studies showing that the average hyporheic exchange velocity is largely controlled by gradients in the hydraulic head at the streambed interface. Furthermore, the results indicate that both the magnitude of the gradients and the distributions of gradients over differently sized geomorphologic features will influence the average of the HEF variables. The established link between the two models can, for example, help to facilitate generalization of HEF. The generalization provided in this study, showed that the dimensionless average exchange velocity increased with an increase in the squared Froude's number, even in streams where the static head variations along the stream bottom were shown to dominate the exchange. The dimensionless average exchange velocity also increased with an increase in the standard deviation in the WSP.

The uncertainty in the cross-validation of the hyporheic RTD was reflected by the finding that the two tested approaches yielded comparable average residence times in only half of the investigated reaches, and that the coefficient of variation agreed to an even smaller extent. Specifically, the HM model resulted in wider distributions and higher average residence times than the tracer test assessment in some of the reaches. The difference could either be attributed to uncertainties in data and evaluation of the two models, or it could be because the two tested approaches generally empathize different parts of the hyporheic RTD. The lower limit of the RTD is constrained in mechanical models by the spatial resolution of the model, and the upper limit of the RTD can be difficult to capture with tracer tests due to a limited window of detection. Moreover, in the three reaches with the highest discharge, low relative roughness, and high Reynolds number, it was not possible to cross-validate the two approaches, even in terms of the average exchange velocity. This result could be attributed either to the notion that HEF consisted of multiple processes in those reaches, such as diffusive turbulence, lateral exchange, or exchange with stagnant surface water, or to a limited window of detection in these three reaches.

This study also included an analysis of how the quantified HEF was distributed over a range of spatial scales, and it led to two conclusions. First, features with wavelengths less than 5 m explained 90% of the hyporheic exchange velocity in the 10 investigated streams, and the inclusion of features with wavelengths smaller than 20 cm, contributed only to a slight increase in exchange velocity in most of the reaches. Second, the static head-driven HEF dominated the dynamic head-driven HEF in all reaches and all measured scales. When scales smaller than the measured scales were included in the investigation, the dynamic head gradients dominated at scales less than approximately 10 cm, in 50% of the reaches. However, this small-scale domination only affected the dynamic contribution to the average hyporheic exchange velocity in two of the reaches, which also had relatively low slopes. Although the spectral investigation revealed uncertainties in the results related to both the HM model formulation and measurement errors, it nevertheless illustrated the improved understanding that can be gained by cross-validating partly independent models. In the future, we suggest that similar studies be performed in different settings using newer, faster, and more accurate elevation measuring techniques.

Data Availability Statement

The data that was collected as part of this study is found in the published resource Morén, I. (2021). Hyporheic exchange flow studies in 10 small streams in south-east Sweden, 2017–2020, HydroShare, https://doi.org/10.4211/hs.af43ffe74d1545f5a918a8af6031c33d. Prepared Matlab codes will be distributed on request by the corresponding author.

Acknowledgments
This study was part of the project "Water flows in the geosphere-biosphere interface (GBI)" funded by the Swedish Radiation Safety Authority, SSM (Dnr SSM2019-1195). The study also received funding from the BONUS Soils2Sea project (Art 185), which was jointly funded by EU's Seventh Programme for research, technological development and demonstration and by The Swedish Environmental Protection Agency. The authors acknowledge Sunna Mjöll, Oscar Wörman, Jenny Forsberg, Olivia Preston, Brian Mojarrad, and Shuang Hao for their invaluable help in the field.

References

Aubeneau, A. F., Martin, R. L., Bolster, D., Shumer, R., Jerolmack, D., & Packman, A. I. (2015). Fractal patterns in river bed morphology produce fractal scaling of water storage times. *Geophysical Research Letters*, *42*, 5309–5315. https://doi.org/10.1002/2015GL064155

Bencala, K. E., Gooseff, M. N., & Kimball, B. A. (2011). Rethinking hyporheic flow and transient storage to advance understanding of stream-catchment connections. *Water Resources Research*, *47*(3). https://doi.org/10.1029/2010wr010066

Bencala, K. E., & Walters, R. A. (1983). Simulation of solute transport in a mountain pool-and-riffle stream: A transient storage model. *Water Resources Research*, *19*(3), 718–724. https://doi.org/10.1029/WR019i003p00718

Boano, F., Camporeale, C., Revelli, R., & Ridolfi, L. (2006). Sinuosity-driven hyporheic exchange in meandering rivers. *Geophysical Research Letters*, *33*, L18406. https://doi.org/10.1029/2006GL027630

Boano, F., Harvey, J. W., Marion, A., Packman, A. I., Revelli, R., Ridolfi, L., & Wörman, A. (2014). Hyporheic flow and transport processes: Mechanisms, models, and biogeochemical implications. *Reviews of Geophysics*, *52*(4), 603–679. https://doi.org/10.1002/2012rg000417

Bottacin-Busolin, A. (2019). Modeling the effect of hyporheic mixing on stream solute transport. *Water Resources Research*, *55*(11), 9995–10011. https://doi.org/10.1029/2019WR025697

Bottacin-Busolin, A., Marion, A., Musner, T., Tregnaghi, M., & Zaramella, M. (2011). Evidence of distinct contaminant transport patterns in rivers using tracer tests and a multiple domain retention models. *Advances in Water Resources*, *34*(6), 737–746. https://doi.org/10.1016/j.advwatres.2011.03.005

Briggs, M. A., Gooseff, M. N., Arp, C. D., & Baker, M. A. (2009). A method for estimating surface transient storage parameters for streams with concurrent hyporheic storage. *Water Resources Research*, *45*(4). https://doi.org/10.1029/2008wr006959

Cardenas, M. B. (2008). Surface water-groundwater interface geomorphology leads to scaling of residence times. *Geophysical Research Letters*, *35*, L08402. https://doi.org/10.1029/2008GL033753

Cardenas, M. B. (2015). Hyporheic zone hydrologic science: A historical account of its emergence and a prospectus. *Water Resources Research*, *51*(5), 3601–3616. https://doi.org/10.1002/2015wr017028

Cardenas, M. B., Wilson, J. L., & Zlotnik, V. A. (2004). Impact of heterogeneity, bed forms, and stream curvature on subchannel hyporheic exchange. *Water Resources Research*, *40*. https://doi.org/10.1029/2004WR003008

Chow, V. T. (1959). *Open-channel hydraulics*. McGraw-Hill Book Company.

Drummond, J. D., Covino, T. P., Aubeneau, A. F., Leong, D., Patil, S., Shumer, R., & Packman, A. I. (2012). Effects of solute breakthrough curve tail truncation on residence time estimates: A synthesis of solute tracer injection studies. *Journal of Geophysical Research*, *117*. https://doi.org/10.1029/2012jg002019

Dufour, S., & Piégay, H. (2009). From the myth of a lost paradise to targeted river restoration: Forget natural references and focus on human benefits. *River Research and Applications*, *25*, 568–581. https://doi.org/10.1002/rra.1239

Elliott, H. A., & Brooks, H. N. (1997a). Transfer of nonsorbing solutes to a streambed with bed forms: Theory. *Water Resources Research*, *33*(1), 123–136. https://doi.org/10.1029/96wr02784

Elliott, H. A., & Brooks, H. N. (1997b). Transfer of nonsorbing solutes to a streambed with bed forms: Laboratory experiments. *Water Resources Research*, *33*(1), 137–151. https://doi.org/10.1029/96wr02783

Fehlman, H. M. (1985). Resistance components and velocity distributions of open channel flows over bedforms, (Ph.D. thesis). Colorado State University.

Gomez-Velez, J. D., & Harvey, J. W. (2014). A hydrogeomorphic river network model predicts where and why hyporheic exchange is important in large basins. *Geophysical Research Letters*, *41*(18), 6403–6412. https://doi.org/10.1002/2014GL061099

Gooseff, M. N., Briggs, M. A., Bencala, K. E., McGlynn, B. L., & Scott, D. T. (2013). Do transient storage parameters directly scale in longer, combined stream reaches? Reach length dependence of transient storage interpretations. *Journal of Hydrology*, *483*, 16–25. https://doi.org/10.1016/j.jhydrol.2012.12.046

Gooseff, M. N., Hall, J. R. O., & Tank, L. J. (2007). *Relating transient storage to channel complexity in streams of varying land use in Jackson Hole, Wyoming* (Vol. 43). Water Resources Research. https://doi.org/10.1029/2005wr004626

Gooseff, M. N., Wondzell, S. M., Haggerty, R., & Anderson, J. (2003). Comparing transient storage modeling and residence time distribution (RTD) analysis in geomorphically varied reaches in the Lookout Creek basin, Oregon, USA. *Advances in Water Resources*, *26*(9), 925–937. https://doi.org/10.1016/s0309-1708(03)00105-2

Grant, S. B., Gomez-Velez, J. D., & Ghisalberti, M. (2018). Modeling the effects of turbulence on hyporheic exchange and local-to-global nutrient processing in streams. *Water Resources Research*, *54*(9), 5883–5889. https://doi.org/10.1029/2018WR023078

Haggerty, R., Wondzell, S. M., & Johnson, M. A. (2002). Power-law residence time distribution in the hyporheic zone of a 2nd-order mountain stream. *Geophysical Research Letters*, *29*(13), 18-1–18-4. https://doi.org/10.1029/2002GL014743

Harvey, J. W., & Bencala, K. E. (1993). The effect of streambed topography on surface-subsurface water exchange in mountain catchments. *Water Resources Research*, *29*(1), 89–98. https://doi.org/10.1029/92wr01960

Harvey, J. W., Conklin, M. H., & Koelsch, R. S. (2003). Predicting changes in hydrologic retention in an evolving semi-arid alluvial stream. *Advances in Water Resources*, *26*(9), 939–950. https://doi.org/10.1016/S0309-1708(03)00085-X

Harvey, J. W., & Wagner, B. J. (2000). Quantifying hydrologic interactions between streams and their subsurface hyporheic zones. In J. B. Jones, & P. J. Mulholland(Eds.), *Streams and ground waters* (pp. 3–44). San Diego: Academic Press. https://doi.org/10.1016/B978-012389845-6/50002-8

Harvey, J. W., Wagner, B. J., & Bencala, K. E. (1996). Evaluating the reliability of the stream tracer approach to characterize stream-subsurface water exchange. *Water Resources Research*, *32*, 2444. https://doi.org/10.1029/96wr01268

Herzog, S. P., Ward, A. S., & Wondzell, S. M. (2019). Multiscale feature-feature interactions control patterns of hyporheic exchange in a simulated. *Headwater Mountain Stream*, *55*(12), 10976–10992. https://doi.org/10.1029/2019WR025763

Hino, M. (1968). Equilibrium-range spectra of sand waves formed by flowing water. *Journal of Fluid Mechanics*, *34*(3), 565–573. https://doi.org/10.1017/S0022112068002089

Hvorslev, M. J. (1951). *Time lag and soil permeability in ground-water observations*. Waterways Experiment Station, Corps of Engineers, U.S. Army.

Johnson, Z. C., Warwick, J. J., & Schumer, R. (2014). Factors affecting hyporheic and surface transient storage in a western U.S. river. *Journal of Hydrology*, *510*, 325–339. https://doi.org/10.1016/j.jhydrol.2013.12.037

Jones, J. B., & Mulholland, P. J. (2000). *Streams and ground waters*. Elsevier.

Keefe, S. H., Barber, L. B., Runkel, R. L., Ryan, J. N., McKnight, D. M., & Wass, R. D. (2004). Conservative and reactive solute transport in constructed wetlands. *Water Resources Research*, *40*, W01201. https://doi.org/10.1029/2003WR002130

19447973, 2021, 12, Downloaded from https://agupubs.onlinelibrary.wiley.com/doi/10.1029/2021WR030248 by Statens Beredning, Wiley Online Library on [28/01/2024]. See the Terms and Conditions (https://onlinelibrary.wiley.com/terms-and-conditions) on Wiley Online Library for rules of use; OA articles are governed by the applicable Creative Commons License

Knapp, J. L. A., & Kelleher, C. (2020). A perspective on the future of transient storage modeling: Let's stop. *Chasing Our Tails*, *56*(3), e2019WR026257. https://doi.org/10.1029/2019WR026257

Lee, A., Aubeneau, A. F., & Cardenas, M. B. (2020). The sensitivity of hyporheic exchange to fractal properties of riverbeds. *Water Resources Research*, *56*(5), e2019WR026560. https://doi.org/10.1029/2019WR026560

Marzadri, A., Tonina, D., McKean, J. A., Tiedemann, M. G., & Benjankar, R. M. (2014). Multi-scale streambed topographic and discharge effects on hyporheic exchange at the stream network scale in confined streams. *Journal of Hydrology*, *519*, 1997–2011. https://doi.org/10.1016/j.jhydrol.2014.09.076

Mojarrad, B. B., Riml, J., Wörman, A., & Laudon, H. (2019). Fragmentation of the hyporheic zone due to regional groundwater circulation. *Water Resources Research*, *55*(2), 1242–1262. https://doi.org/10.1029/2018WR024609

Morén, I., Wörman, A., & Riml, J. (2017). Design of remediation actions for nutrient mitigation in the hyporheic zone. *Water Resources Research*, *53*, 8872–8899. https://doi.org/10.1002/2016WR020127

O'Connor, B. L., & Harvey, J. W. (2008). Scaling hyporheic exchange and its influence on biogeochemical reactions in aquatic ecosystems. *Water Resources Research*, *44*(12). https://doi.org/10.1029/2008WR007160

Packman, A. I., Salehin, M., & Zaramella, M. (2004). Hyporheic exchange with gravel beds: Basic hydrodynamic interactions and bedform-induced advective flows. *Journal of Hydraulic Engineering*, *130*(7), 647–656. https://doi.org/10.1061/(asce)0733-9429(2004)130:7(647)

Passalacqua, P., Belmont, P., Staley, D. M., Simley, J. D., Arrowsmith, J. R., Bode, C. A., et al. (2015). Analyzing high-resolution topography for advancing the understanding of mass and energy transfer through landscapes: A review. *Earth-Science Reviews*, *148*, 174–193. https://doi.org/10.1016/j.earscirev.2015.05.012

Riml, J., & Wörman, A. (2011). Response functions for in-stream solute transport in river networks. *Water Resources Research*, *47*(6). https://doi.org/10.1029/2010wr009412

Riml, J., Wörman, A., Kunkel, U., & Radke, M. (2013). Evaluating the fate of six common pharmaceuticals using a reactive transport model: Insights from a stream tracer test. *Science of the Total Environment*, *458–460*, 344–354. https://doi.org/10.1016/j.scitotenv.2013.03.077

Runkel, R. L. (1998). One-Dimensional Transport with Inflow and Storage (OTIS): A Solute Transport Model for Streams and Rivers. U.S. Geological Survey Water-Resources Investigations Report, 98-4018, 73. https://doi.org/10.3133/wri984018

Runkel, R. L. (2002). A new metric for determining the importance of transient storage. *Journal of the North American Benthological Society*, *21*(4), 529–543. https://doi.org/10.2307/1468428

Runkel, R. L. (2015). On the use of rhodamine WT for the characterization of stream hydrodynamics and transient storage. *Water Resources Research*, *51*, 6125–6142. https://doi.org/10.1002/2015WR017201

Salehin, M., Packman, A. I., & Wörman, A. (2003). Comparison of transient storage in vegetated and unvegetated reaches of a small agricultural stream in Sweden: Seasonal variation and anthropogenic manipulation. *Advances in Water Resources*, *26*(9), 951–964. https://doi.org/10.1016/S0309-1708(03)00084-8

Sawyer, A. H., Bayani Cardenas, M., & Buttles, J. (2011). Hyporheic exchange due to channel-spanning logs. *Water Resources Research*, *47*, W08502. https://doi.org/10.1029/2011WR010484

Schmadel, N. M., Ward, A. S., Kurz, M. J., Fleckenstein, J. H., Zarnetske, J. P., Hannah, D. M., et al. (2016). Stream solute tracer timescales changing with discharge and reach length confound process interpretation. *Water Resources Research*, *52*(4), 3227–3245. https://doi.org/10.1002/2015WR018062

Stewardson, M. J., Datry, T., Lamouroux, N., Pella, H., Thommeret, N., Valette, L., & Grant, S. B. (2016). Variation in reach-scale hydraulic conductivity of streambeds. *Geomorphology*, *259*, 70–80. https://doi.org/10.1016/j.geomorph.2016.02.001

Stoica, P., & Moses, R. L. (1997). *Introduction to spectral analysis*. Prentice Hall.

Stonedahl, S. H., Harvey, J. W., Detty, J., Aubeneau, A., & Packman, A. I. (2012). Physical controls and predictability of stream hyporheic flow evaluated with a multiscale model. *Water Resources Research*, *48*(10), W10513. https://doi.org/10.1029/2011wr011582

Stonedahl, S. H., Harvey, J. W., & Packman, A. I. (2013). *Interactions Between Hyporheic Flow Produced by Stream Meanders, Bars, and Dunes* (Vol. 49). Water Resources Research. https://doi.org/10.1002/wrcr.20400

Stonedahl, S. H., Harvey, J. W., Wörman, A., Salehin, M., & Packman, A. I. (2010). *A Multiscale Model for Integrating Hyporheic Exchange From Ripples to Meanders* (Vol. 46). Water Resources Research. https://doi.org/10.1029/2009wr008865

Tonina, D., & Buffington, J. M. (2007). Hyporheic exchange in gravel bed rivers with pool-riffle morphology: Laboratory experiments and three-dimensional modeling. *Water Resources Research*, *43*(1). https://doi.org/10.1029/2005wr004328

Tonina, D., & Buffington, J. M. (2011). Effects of stream discharge, alluvial depth, and bar amplitude on hyporheic flow in pool-riffle channels. *Water Resources Research*, *47*(8). https://doi.org/10.1029/2010wr009140

Tóth, J. (1963). A theoretical analysis of groundwater flow in small drainage basins. *Journal of Geophysical Research*, *68*(16), 4795–4812. https://doi.org/10.1029/JZ068i016p04795

Turcotte, D. L. (1992). *Fractals and chaos in geology and geophysics*. Great Britain: Cambridge University Press.

Ward, A. S., Kelleher, C. A., Mason, S. J. K., Wagener, T., McIntyre, N., McGlynn, B., et al. (2017). A software tool to assess uncertainty in transient-storage model parameters using Monte Carlo simulations. *Freshwater Science*, *36*(1), 195–217. https://doi.org/10.1086/690444

Ward, A. S., & Packman, A. I. (2019). Advancing our predictive understanding of river corridor exchange. *Water*, *6*(1), e1327. https://doi.org/10.1002/wat2.1327

Ward, J., Tockner, K., Uehlinger, U., & Malard, F. (2001). Understanding natural patterns and processes in river corridors as the basis for effective river restoration. *Regulated Rivers Research & Management*, *17*, 311–323. https://doi.org/10.1002/rrr.646

Wondzell, S. M., Herzog, S. P., Gooseff, M. N., Ward, A. S., & Schmadel, N. M. (2019). Geomorphic controls on hyporheic exchange across scales—Watersheds to particles. In *Reference module in Earth systems and environmental sciences*. Elsevier.

Woodget, A. S., Austrums, R., Maddock, I. P., & Habit, E. (2017). Drones and digital photogrammetry: From classifications to continuums for monitoring river habitat and hydromorphology. *WIREs Water*, *4*(4), e1222. https://doi.org/10.1002/wat2.1222

Wörman, A., Packman, A. I., Johansson, H., & Jonsson, K. (2002). Effect of flow-induced exchange in hyporheic zones on longitudinal transport of solutes in streams and rivers. *Water Resources Research*, *38*(6). https://doi.org/10.1029/2001wr001175

Wörman, A., Packman, A. I., Marklund, L., Harvey, J. W., & Stone, S. (2007). Fractal topography and subsurface water flow form from fluvial bedforms to the continental shield. *Geophysical Research Letters*, *34*. https://doi.org/10.1029/2007gl029426

Wörman, A., Packman, A. I., Marklund, L., Harvey, J. W., & Stonedahl, S. H. (2006). Exact three-dimensional spectral solution to surface-groundwater interactions with arbitrary surface topography. *Geophysical Research Letters*, *33*. https://doi.org/10.1029/2006gl025747

19447973, 2021, 12, Downloaded from https://agupubs.onlinelibrary.wiley.com/doi/10.1029/2021WR030248 by Statens Beredning, Wiley Online Library on [28/01/2024]. See the Terms and Conditions (https://onlinelibrary.wiley.com/terms-and-conditions) on Wiley Online Library for rules of use; OA articles are governed by the applicable Creative Commons License

Wörman, A., & Wachniew, P. (2007). Reach scale and evaluation methods as limitations for transient storage properties in streams and rivers. *Water Resources Research*, *43*, W10405. https://doi.org/10.1029/2006WR005808

Zarnetske, J. P., Gooseff, M. N., Brosten, T. R., Bradford, J. H., McNamara, J. P., & Bowden, W. B. (2007). Transient storage as a function of geomorphology, discharge, and permafrost active layer conditions in Arctic tundra streams. *Water Resources Research*, *43*(7). https://doi.org/10.1029/2005WR004816

Reference From the Supporting Information

Welch, P. (1967). The use of fast Fourier transforms for the estimation of power spectra: A method based on time averaging over short, modified periodograms. *IEEE Transactions on Audio and Electroacoustics*, *15*(2), 70–73. https://doi.org/10.1109/TAU.1967.1161901

19447973, 2021, 12, Downloaded from https://agupubs.onlinelibrary.wiley.com/doi/10.1029/2021WR030248 by Statens Beredning, Wiley Online Library on [28/01/2024]. See the Terms and Conditions (https://onlinelibrary.wiley.com/terms-and-conditions) on Wiley Online Library for rules of use; OA articles are governed by the applicable Creative Commons License